FINE-SCALE RADAR OBSERVATIONS OF OROGRAPHIC PRECIPITATION FEATURES DURING A WASATCH MOUNTAIN WINTER STORM

by

Leah Suzanne Campbell

A thesis submitted to the faculty of
The University of Utah
in partial fulfillment of the requirements for the degree of

Master of Science

Department of Atmospheric Sciences

The University of Utah

December 2013

THE UNIVERSITY OF UTAH GRADUATE SCHOOL

STATEMENT OF THESIS APPROVAL

The thesis of **Leah Suzanne Campbell**

has been approved by the following supervisory committee members:

William J. Steenburgh	, Chair	**8/15/13** Date Approved
John D. Horel	, Member	**8/15/13** Date Approved
Timothy J. Garrett	, Member	**8/15/13** Date Approved

and by **Kevin Perry** , Chair of

the Department of **Atmospheric Sciences**

and by David B. Kieda, Dean of The Graduate School.

ABSTRACT

Fine-scale spatiotemporal variations in orographic precipitation pose a major challenge for weather prediction in mountainous regions. Here we use ground-based X-band radar observations collected during IOP6 of the Storm Chasing Utah Style Study (SCHUSS) to provide an illustrative example of such variations during a cold-frontal passage over the Wasatch Mountains of northern Utah. Emphasis is placed on precipitation features in and around Little Cottonwood Canyon (LCC), which cuts orthogonally eastward into the Wasatch Mountains. This work also demonstrates the potential for improving weather analysis and forecasting of such variations in LCC using a gap-filling radar.

Precipitation during the weakly stratified prefrontal storm stage of IOP6 featured a wave-like barrier-scale reflectivity maximum along the Wasatch Crest that extended weakly westward and upstream over the transverse ridges flanking LCC. These characteristics appeared to reflect a veering wind profile, which produced southwesterly flow over the ridges flanking LCC but cross-barrier westerly flow further aloft. Sublimation within dry subcloud air further diminished radar reflectivities over lower LCC. The cold front was associated with stronger reflectivities over lower LCC and at lower-to-mid elevations along the northwest-facing canyon wall, consistent with shallow, northwesterly upslope flow. Eventually, shallow precipitating cells developed in the moist-neutral postfrontal flow, with the

depth, coverage and intensity of these cells increasing from over the Salt Lake Valley to upper LCC.

TABLE OF CONTENTS

ACKNOWLEDGEMENTS

I thank committee chair, Dr. Jim Steenburgh for his much appreciated guidance and perspective, and committee members, John Horel and Tim Garrett for their availability and advice during the writing of this thesis. Comments from Jon Zawislak, Larry Dunn and Ralph Patterson improved the manuscript, and advice, troubleshooting, and support from my fellow graduate students were integral to the research process. Thanks to Josh Wurman and the staff at the Center for Severe Weather Research for the use of and support for the Doppler on Wheels 6 during the SCHUSS field program, and to Tim Garrett for providing snowflake photographs from the HYVIS camera at Alta. Jon Zawislak, Joe Young, Gabe Susca-Lopata, and Trevor Alcott operated the Doppler on Wheels 6 during the event explored in this thesis. I gratefully acknowledge the provision of datasets, software, and/or computer time and services by NCDC, NCEP, NCAR, Unidata, MesoWest, the University of Wyoming, and the University of Utah Center for High Performance Computing. This material is based upon work supported by National Science Foundation Grants AGS-0938611 and AGS-1262090. Any opinions, findings, conclusions or recommendations expressed in this thesis are those of the author and do not necessarily reflect the views of the National Science Foundation.

CHAPTER 1

INTRODUCTION

Fine-scale spatiotemporal variations in precipitation over areas of highly three-dimensional topography pose a significant challenge for weather and climate prediction, hydrologic forecasting, avalanche mitigation, and winter road maintenance in mountainous regions. Interactions between the large-scale flow, regional topography, and local terrain features can create dramatic variations in precipitation rate and structure over small spatial scales during individual storms (Sinclair et al. 1997; Smith et al. 2003; Molinié et al. 2012) as well as over climatological time periods (e.g., Frei and Schär 1998; Anders et al. 2007). Although much of the research examining orographic precipitation has concentrated on barrier-scale effects, especially windward enhancement processes, the influence of smaller-scale topographic features (e.g., ridge-valley corrugations) and more complex terrain geometries has received less attention (Neiman and Ralph 2004; Rotunno and Houze 2007; Minder et al. 2008).

A rich spectrum of dynamical and microphysical processes affect orographic precipitation [see Roe (2005), Smith (2006), Houze (2012), Colle et al. (2013), and Stoelinga et al. (2013) for recent reviews]. These effects vary with the size and shape of the terrain, the time scales controlling the growth and fallout of

precipitation particles, and the dynamics and thermodynamics of the incipient airflow (Houze 2012). Over the western United States, many orographic storms evolve through *stable*, *neutral* (a.k.a. *frontal*), and *unstable* stages (e.g., Hobbs 1975; Marwitz 1980; Cooper and Saunders 1980; Long et al. 1990; Sassen et al. 1990; Medina et al. 2007). The stable and unstable stages are roughly analogous to the "flow around" and "flow over" regimes emphasized by Rotunno and Houze (2007). The so-called neutral or frontal stage can feature a sharp cold-frontal passage (Long et al. 1990; Sassen et al. 1990), a gradual transition in storm structure (Marwitz 1980), or a surge of low equivalent potential temperature (θ_e) air aloft that destabilizes the prefrontal environment, leading to convection (Reynolds and Kuciauskas 1988; Steenburgh 2003).

During the stable stage, the low-level flow is often blocked, resulting in an upstream pool of stagnant air or a barrier jet, which effectively extends the mountain upstream and lessens the slope of the obstacle. Increased low-level stability due to diabatic cooling from sublimation or evaporation can also contribute to flow blocking, as has been observed upstream of the Wasatch Mountains of northern Utah (Colle et al. 2005; Cox et al. 2005), and create down-slope or down-valley flow within canyons and valleys (Hill 1978; Bousquet and Smull 2003; Steiner et al. 2003). The ascent of the incident air over blocked flow can enhance precipitation as much as 100–150 km upstream of the initial mountain slope (Peterson et al. 1991; Houze et al. 2001). In some cases, strong vertical wind shear and turbulence near the top of the blocked airmass may contribute to precipitation generation (Medina et al. 2005; Houze and Medina 2005).

Precipitation processes during the stable stage can also be influenced by barrier- and subbarrier-scale mountain waves, the latter produced by ridge-valley corrugations in the topography. While ascent over a barrier has been shown to produce increased cloud liquid water contents (e.g., Heggli and Rauber 1988), Bruintjes et al. (1994) found that small-scale ridges produced gravity waves downstream that featured stronger ascent and higher cloud liquid water contents extending throughout deeper layers of the atmosphere than that observed over the initial barrier. This results in dramatic small-scale precipitation gradients, in some cases increasing precipitation over downstream ridges (Reinking et al. 2000; Klimowski et al. 1998).

The structure of mountain waves and their influence on precipitation depends on barrier width and the scale of ridge-valley corrugations, as well as dynamical and microphysical factors. Colle (2004) showed that the reduced upstream tilt of gravity waves over narrow barriers (~25 km half width) results in precipitation fallout over the crest and spillover to the lee. Colle (2008) used two-dimensional simulations to show that a series of windward ridges can enhance precipitation over each ridge crest by a factor of 2–3 when the ridge spacing is relatively small (~20km) and there is strong cross-barrier flow. Over the Cascade Mountains during IMPROVE-2, a synergistic effect was found between barrier-scale mountain waves produced by the midlevel cross-barrier flow and low-level mountain waves formed by along-barrier flow over ridge-valley corrugations. Together, these mountain waves were associated with increased radar reflectivity,

cloud liquid water production, and hydrometeor mixing ratios over the subbarrier-scale windward ridges (Garvert et al. 2005, 2007).

During the frontal stage, precipitation structure and cold-frontal behavior are dependent on environmental stability and terrain geometry (Egger and Hoinka 1992). Many cold fronts weaken and slow as they ascend the windward slope (e.g., Gross 1994; Schumacher et al. 1996; Bond et al. 2005), however low-level terrain blocking and deflection can have frontogenetical effects upstream of the barrier. Yu and Smull (2000) and Colle et al. (2002) found that terrain-blocked prefrontal southerly flow ahead of a land-falling cold front that was oriented at an acute angle to the mountain barrier helped contribute to frontal intensification and the genesis of a narrow cold-frontal rainband upstream of the coastal mountains of California. In more complex terrain, Colle et al. (1999) showed that the retardation and deflection of a land-falling front upstream and around the quasicircular Olympic Mountains resulted in intensification of the front upstream and around the mountain range. Diabatic effects can also modify cold-frontal behavior: Schultz and Trapp (2003) showed that dry subcloud air modified the structure and precipitation gradients of a forward-tilting cold front in the Salt Lake Valley (SLV) of northern Utah.

The postfrontal environment is frequently characterized by decreased stability and orographically initiated or enhanced convection behind the cold front (e.g., Hobbs 1975). Reynolds and Kuciauskas (1988) and Peterson et al. (1991) found that following cold-frontal passage in the Sierra Nevada, dry air tends to move in aloft with the resulting potential instability released as shallow convection when

the flow surmounts the mountain barrier. Over the Oregon Cascades, Medina et al. (2007) found that the "late sector" of extra-tropical cyclones, analogous to the unstable stage, generally consists of shallow convective echoes, which broaden as they move over the mountain barrier. This was also observed during IMPROVE-II when postfrontal convective cells strengthened and upstream precipitation became more persistent during flow over the Cascade Mountains (Woods et al. 2005).

In this thesis we investigate the evolution of a winter storm across the complex topography of northern Utah, with emphasis on precipitation features over the central Wasatch Mountains (Fig. 1a) and Little Cottonwood Canyon (LCC, Fig. 2a). The central Wasatch Mountains, east of the Salt Lake Valley (SLV), contain a complex system of east-west oriented canyons (including LCC) and transverse ridges oriented orthogonal to the predominantly north–south oriented Wasatch Crest. In contrast, the northern Wasatch Mountains are more linear and create a steep, generally homogenous barrier to the east of the Great Salt Lake and north of the SLV.

Figure 2a illustrates the topographic features of the central Wasatch Mountains and the glacially carved LCC. Although the Wasatch Crest forms a hydrological divide near the eastern termini of LCC, Big Cottonwood Canyon, and Mill Creek Canyon, the highest terrain is found farther west along the Alpine and Cottonwood Ridges, which flank LCC and extend westward towards the SLV. Lone Peak [3430 m above mean sea level (MSL); all subsequent elevations MSL unless otherwise specified] and Twin Peaks (3453 m) create the westernmost abutments

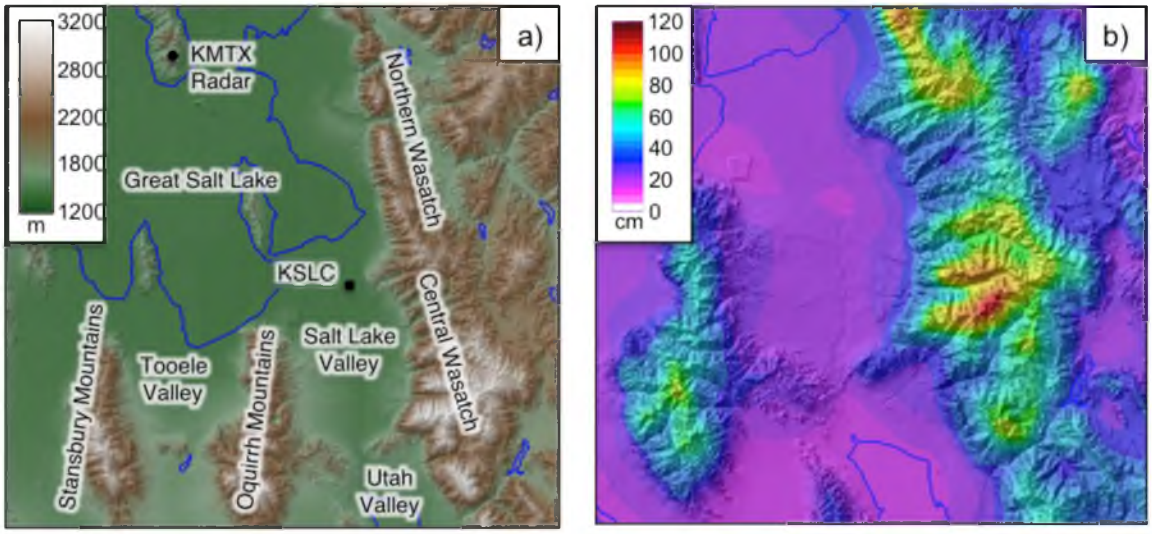

Fig. 1. (a) Topography and landmarks of the study region. (b) Mean cool-season precipitation (cm, following scale at left). Data source: PRISM Climate Group, Oregon State University, http://prism.oregonstate.edu.

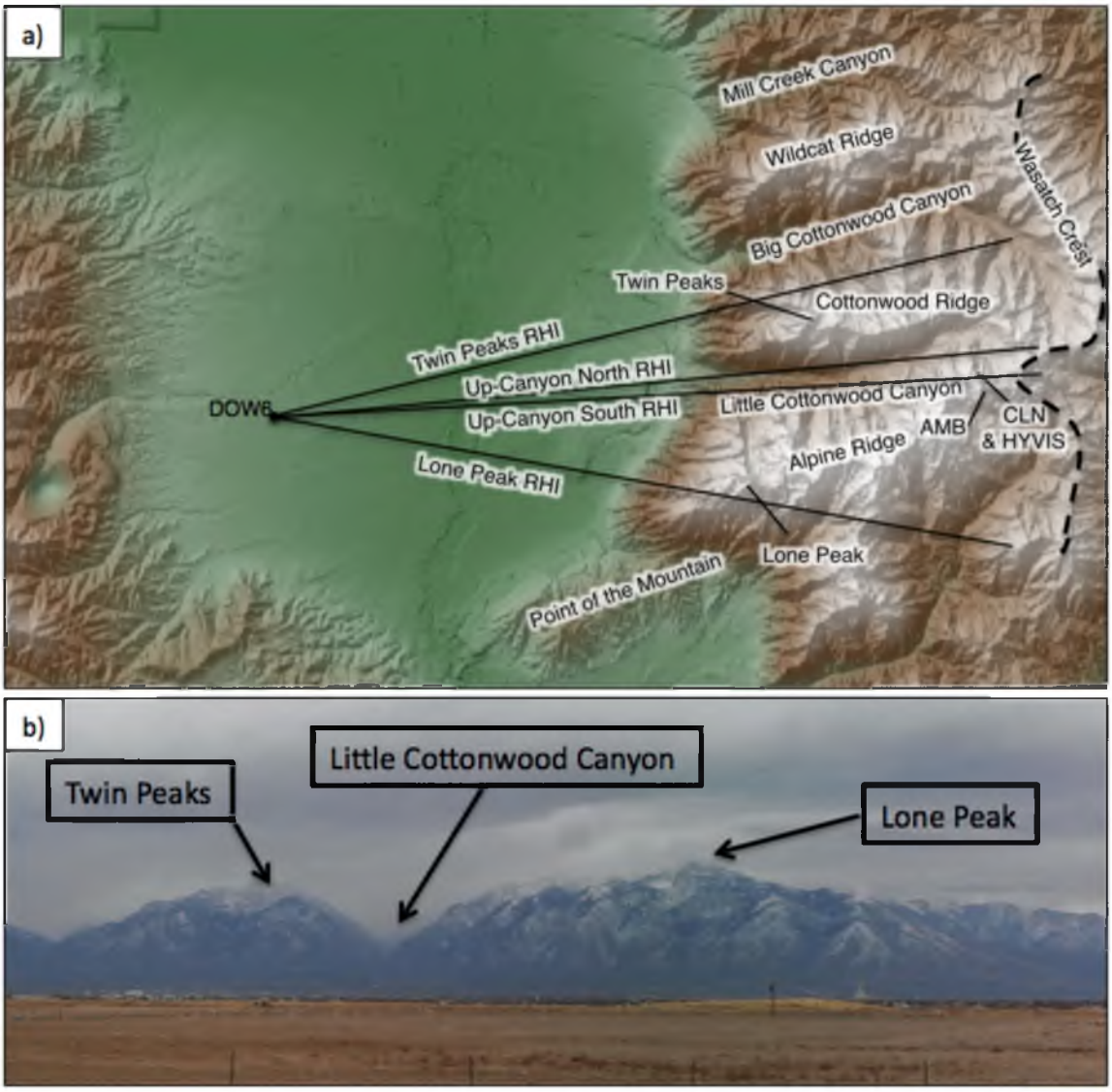

Fig. 2. (a) Topography of the central Wasatch Mountains, including locations of range height indicator (RHI) scans in and around LCC. Dashed line denotes the hydrological divide, or Wasatch Crest. (b) View of LCC and surrounding topography from the DOW6 site.

of the Alpine and Cottonwood Ridges, respectively, and dominate the SLV skyline (Fig. 2b).

Dramatic climatological gradients in cool-season (Nov–Apr) precipitation are found over the central Wasatch Mountains (Fig. 1b, Dunn 1983). In upper LCC, Alta Ski Area (2661 m) averages over 96 cm of snow water equivalent (SWE) during the cool season, whereas Salt Lake City International Airport (KSLC; 1286 m; see Fig. 1a for location) in the northern SLV averages 23.3 cm, more than a fourfold difference (Western Regional Climate Center, 2013). Although there is a strong correlation between precipitation and elevation, the precipitation estimates produced by the PRISM Climate Group at Oregon State University (Daly et al. 1994) and presented in Fig. 1b suggest that precipitation is greatest over LCC and the adjoining Alpine and Cottonwood ridges, with less precipitation at comparable elevations in other portions of the central Wasatch Mountains.

The winter storm examined here was sampled during Intensive Observing Period 6 (IOP6; 0900 UTC 12 November to 0400 UTC 13 November 2011) of the Storm Chasing Utah Style Study (SCHUSS), enabling the use of mobile dual-polarization X-band Doppler radar and other assets. During IOP6, the Doppler on Wheels 6 (DOW6) operated from the southwest corner of the SLV (see Fig. 2a for location) where the mostly unobstructed view up and around LCC allowed for the detailed observation of precipitation features that were shaped by multiscale mountain waves, front-mountain interactions, and convective processes. These features can dramatically affect the gradient of precipitation intensity along State Route 210 (SR-210), the heavily used highway that runs the length of LCC, providing

the only access to two of Utah's most popular ski resorts, and is plagued by very high snow avalanche hazard and treacherous winter driving conditions (Little Cottonwood Canyon SR-210 Transportation Study, 2006). Weather and avalanche forecasters cannot currently sufficiently resolve these fine-scale spatiotemporal gradients in precipitation intensity using the existing Nexrad radar coverage because of issues such as beam blockage by the complex terrain of the Wasatch Mountains, overshooting of low-level precipitation features, and the longer wavelength of the S-Band Nexrad radar (see Fig. 1a for location). This thesis illustrates the potential for using ground-based X-band Doppler radar to fill gaps in Nexrad coverage and improve weather prediction, avalanche mitigation, and winter road maintenance efforts in and around LCC.

CHAPTER 2

DATA AND METHODS

Doppler on Wheels

High-resolution radar scans from Doppler on Wheels 6 (DOW6), an X-band (3.2 cm wavelength) dual-polarized Doppler weather radar developed by the Center for Severe Weather Research (Wurman et al. 1997) and operated by students from the University of Utah, are the cornerstone of this analysis. During IOP6, DOW6 operated near the southwest corner of the SLV at 1508 m — about 200 m above the lowest point in the valley — and had a mostly unobstructed view up LCC (Fig. 2). The continuous scanning strategy included plan position indicator (PPI) scans at approximately 1° intervals between 0.5° and 13.7° and range height indicator (RHI) scans over LCC, the surrounding central Wasatch Mountains, and the eastern SLV. DOW6 operated between 1405 – 0402 UTC 12–13 November 2011.

Software programs SOLO and XLTRSII (Oye et al. 1995) were used to visualize, process, and translate the DOW6 data. Processing and quality control included the reorientation of PPI and RHI scans relative to true north, the application of a Normalized Coherent Power (NCP) minimum of 0.25, and the removal of range gates exhibiting both low velocity and high reflectivity values as ground clutter. A low bias in radar reflectivity may exist down-beam of topographic

features that generate partial beam blockage (James et al. 2000), however, these range gates were not removed. Velocity unfolding was performed at a Nyquist velocity of 19.6 m s^{-1}. Interpolation to a Cartesian grid was completed at a 75 m horizontal and 50 m vertical resolution, factoring in a 4/3 earth radius assumption and standard atmospheric refraction conditions (Rinehart 1997).

Time-mean reflectivity and velocity RHIs presented in this paper reflect the average reflectivity or velocity value of each range gate for the specified time period. Composite time-mean reflectivity PPIs are produced by first creating time-mean reflectivity PPIs for each scan angle between 3.2° and 13.7°, then calculating the maximum value for each range gate between all scan angles of the time-mean PPIs. For both RHIs and PPIs the averaging process eliminates range gates with undefined values from the time-mean calculation, and range gates with fewer than 5 real values for the time period are assigned an undefined value.

The X-band hydrometeor typing algorithm follows Dolan and Rutledge (2009), which uses horizontal radar reflectivity, dual-polarization variables such as differential reflectivity, specific differential phase, and correlation coefficient, as well as vertical temperature profiles (this analysis used soundings launched from KSLC and the DOW6 site), to determine hydrometeor type using a fuzzy-logic-based approach. Schneebeli et al. (2013) recently used this algorithm to examine the microphysical processes contributing to precipitation in the Swiss Alps. The Dolan and Rutledge (2009) algorithm uses a T-matrix scattering model with seven modeled hydrometeor types (vertically aligned ice, ice crystals, aggregates, low-density graupel, high-density graupel, drizzle/light rain, and rain), of which four

were predominant during IOP6: (1) *ice crystals* are assumed to have diameters smaller than 1.5 mm, small axis ratios of 0.1 to 0.3, densities near that of pure ice (0.4 to 0.9 g cm^{-1}), and temperatures between –40° and –10° C; (2) *aggregates* are modeled as conglomerates of semispherical, randomly oriented ice crystals with diameters of 1–12 mm, axis ratios of 0.2 to 0.9, densities between 0.1 and 0.2 g cm^{-1}, and temperatures between –15° and 5° C; (3) *drizzle/light rain* is composed of small spherical droplets with diameters from 0.3 to 0.55 mm and temperatures above 0° C; and (4) *low-density graupel* is assumed to have axis ratios of 0.5–1.25, densities between 0.25 g cm^{-2} and 0.55 g cm^{-2}, and temperatures of –20° to 0°C. The low-density graupel temperature range was modified from the range assigned in the Dolan and Rutledge (2009) algorithm (-20° to -10°C), to reflect our own observations of partially to fully rimed crystals and small graupel at temperatures up to 0° C during wintertime orographic precipitation in the central Wasatch Mountains. The relatively broad spectrum of riming associated with low-density graupel is related to the cloud liquid water contents and residence times that are associated with vertical motion.

Specific differential phase, which is dependent on axis ratio and particle concentration and is used most commonly for the detection of heavy rain, was not available for much of IOP6, therefore the algorithm used in this paper does not include this variable. The use of specific differential phase may have helped resolve a misclassification (discussed later in this thesis) between aggregates and low-density graupel (which have similar sizes, axis ratios, and temperature ranges), as

the specific differential phase range for aggregates (0 to 0.3) is much more specific than that for low-density graupel (-1.4 to 2.8).

The hydrometeor type RHIs presented identify the predominant hydrometeor type observed at each range gate during the specified time interval, and we present snowflake images captured by a hydrometeor videosonde (HYVIS; Murakami and Matsuo 1990) snowflake camera system at Alta Ski Area for comparison. The motion-activated camera takes one-dimensional photographs of snowflakes as they fall through a cylindrical tube, cataloguing them by timestamp. While the quality of these images is variable, the shape and size of the silhouettes allow us to subjectively classify the snow crystals. The HYVIS system was located in a sheltered grove of trees at about 2990 m, ~360 m horizontally from the Up-Canyon South RHI scan, ~1000 m horizontally from the Up-Canyon North RHI scan, and ~340 m horizontally from the Alta-Collins (CLN) weather station (Fig. 2a). The hydrometeor type algorithm was run using the Up-Canyon South RHI for all time periods except for 1430–1700 UTC, when the Up-Canyon South RHI was not available and the Up-Canyon North RHI was used instead.

Supplemental Meteorological Data

While the DOW6 provided higher resolution radar observations, regional-scale precipitation features were examined using base (0.5°) reflectivity scans from the KMTX National Weather Service Weather Surveillance Radar-1988 Doppler (WSR-88D; Crum and Alberty 1993). KMTX is located on Promontory Point, a major peninsula of the Great Salt Lake, at 2004 m — about 500 m above the DOW6 site and

about 700 m above the valley floor (Fig. 1a). KMTX data presented in this thesis was smoothed using a moving average filter with a span of 10 data points.

Upper-air soundings include those taken operationally at KSLC at 0000 UTC (~2315 UTC launch time), as well as additional Graw GPS-based soundings launched from the DOW6 site by University of Utah students. Profiles of squared dry (N_d^2) and moist (N_m^2) Brunt-Väisälä frequencies were calculated following Durran and Klemp (1982), and were smoothed using a moving average filter with a span of 10 data points. Froude number (U/NH) was calculated assuming a north–south oriented barrier with a homogeneous barrier height (H) of 1800 m. The cross-barrier wind U was calculated using the westerly component of wind speed. N_d and N_m were used as N for the dry (F_d) and moist (F_m) Froude numbers, respectively. Time-height cross-sections and plan-view analyses from the Rapid Update Cycle version 2 (RUC2; Benjamin et al. 1998), available hourly at 13-km grid spacing, were also used to assess synoptic conditions. Surface observations, including hourly snow water equivalent (SWE) amounts, were obtained from the Mesowest cooperative networks, which provide high-density weather observations in the west and across the United States (Horel et al. 2002).

CHAPTER 3

RESULTS

Overview of IOP6

During the event sampled by IOP6, a mobile upper-level shortwave trough moved across northern Utah from 0900 UTC 12 November to 0400 UTC 13 November 2011, with the accompanying surface cold front passing KSLC at 1940 UTC 12 November and entering LCC at 2030 UTC 12 November. We have divided IOP6 into three stages: prefrontal, frontal, and postfrontal, and, due to the gradual progression of the cold front across the study area, have defined a later time of transition to the frontal stage in LCC compared to KSLC. The lengthy prefrontal stage (0900–1940 UTC 12 November at KSLC and 0900–2030 UTC 12 November in LCC) featured a weakly stratified atmosphere with a dry (i.e., relative humidity < 80%) subcloud layer below ~750 hPa (Fig. 3). Over the SLV, winds veered with height from southerly or southeasterly near the surface (not evident in the Rapid Update Cycle 2 (RUC2) analysis presented in Fig. 3) to westerly above crest-level (~700 hPa). With the passage of the shallow cold front (frontal stage; 1940–2100 UTC 12 November at KSLC and 2030–2130 12 November in LCC) the flow below crest level shifted to northwesterly and destabilized, whereas westerly flow persisted above crest level (~700 hPa). Later, in the postfrontal stage (2100–0400 UTC 12–13

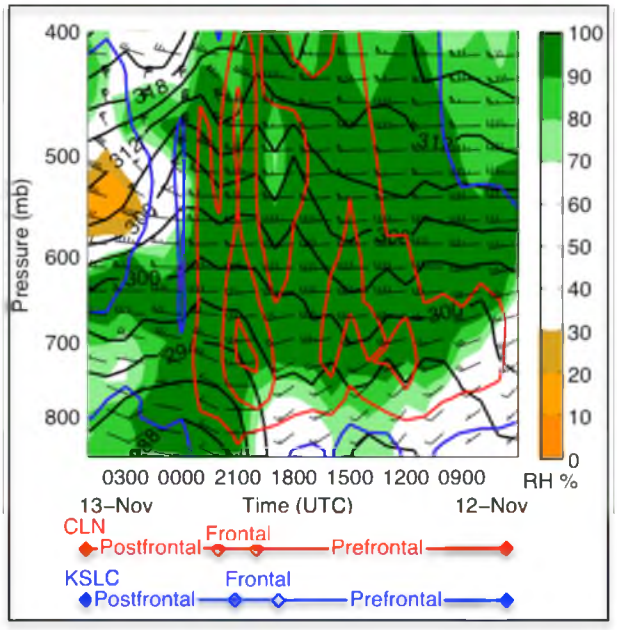

Fig. 3. RUC2 KSLC time–height section of θ_e (black contours every 3 K), pressure vertical velocity [contours every 1 Pa s^{-1} with red (blue) indicating upward (downward) motion], wind (full and half barbs denote 5 and 2.5 m s^{-1}, respectively), and relative humidity (%, shaded following scale at right). Times of prefrontal, frontal, and postfrontal stages for CLN (red) and KSLC (blue) are annotated at bottom.

November at KSLC and 2130–0400 UTC in LCC) drier, more stable air moved into northern Utah.

The event produced 6 in (15 cm) of snow and 0.75 in (1.9 cm) of snow water equivalent (SWE) at CLN in upper LCC and 0.19 in (0.47 cm, in the form of rain or wet snow) of SWE at KSLC in the SLV (see Fig. 1a and Fig. 2a for locations). Although CLN recorded measurable SWE during all three storm stages, KSLC did not record any measurable SWE during the prefrontal and frontal stages, with all the measureable precipitation falling during the postfrontal stage (Fig. 4). The remainder of this chapter describes the structure and evolution of precipitation as observed by DOW6 during the three storm stages, with an emphasis on LCC.

Prefrontal Stage

DOW6 operations for IOP6 commenced at 1405 UTC 12 November near the midpoint of the prefrontal stage. At 1500 UTC 12 November, the 500-hPa trough axis and vorticity maximum were over Idaho, with the surface cold front and leading edge of the accompanying 700-hPa baroclinic zone penetrating into northwest Utah [Fig. 5a,b (surface front not shown)]. The prefrontal atmosphere over the SLV featured a near moist-adiabatic lapse rate from the surface to 630 hPa and a dry subcloud airmass with dewpoint depressions as large as 9.5°C at 781 hPa (Fig. 6). Winds veered from southeasterly at the surface to southwesterly near crest-level (~700 hPa) and west-southwesterly further aloft. This veering wind profile likely reflects weak prefrontal warm advection combined with the channeling of flow in the SLV, which is consistent with the unsaturated conditions, the relatively large N_d, and the low (generally < 1) F_d below crest level (~700 hPa).

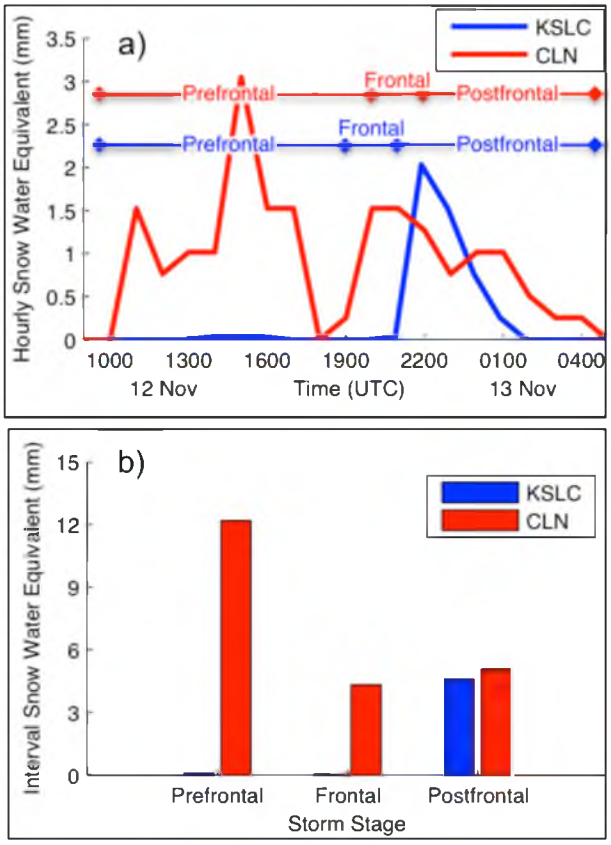

Fig. 4. (a) Hourly accumulated precipitation (SWE, mm) at KSLC and CLN with major stages annotated. (b) Accumulated precipitation for each storm stage (SWE, mm) at KSLC and CLN.

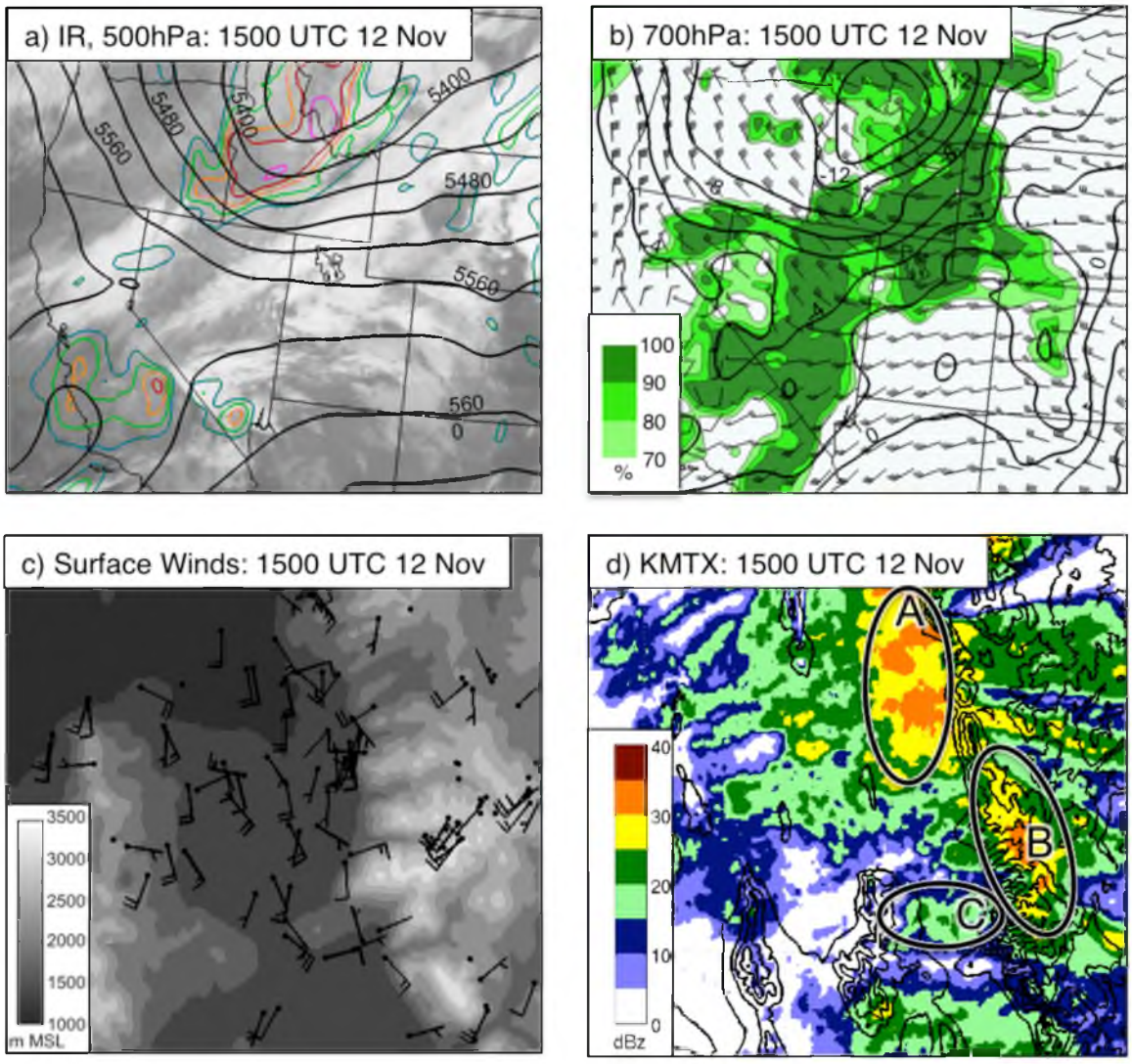

Fig. 5. Environmental conditions for 1500 UTC 12 November. (a) RUC2 500-hPa geopotential height (black contours every 60 m) and absolute vorticity (colored contours every 4×10^{-5} s^{-1}), and infrared satellite image. (b) RUC2 700-hPa temperature (black contours every 2°C), wind (full and half barbs denote 5 and 2.5 m s^{-1}, respectively), and relative humidity (%, shaded following scale at lower left). (c) MesoWest wind surface observations [wind barbs as in (b)] and terrain elevation (m, shaded following scale at lower left). (d) KMTX lowest-elevation angle (0.5°) base reflectivity (shaded following scale at lower left).

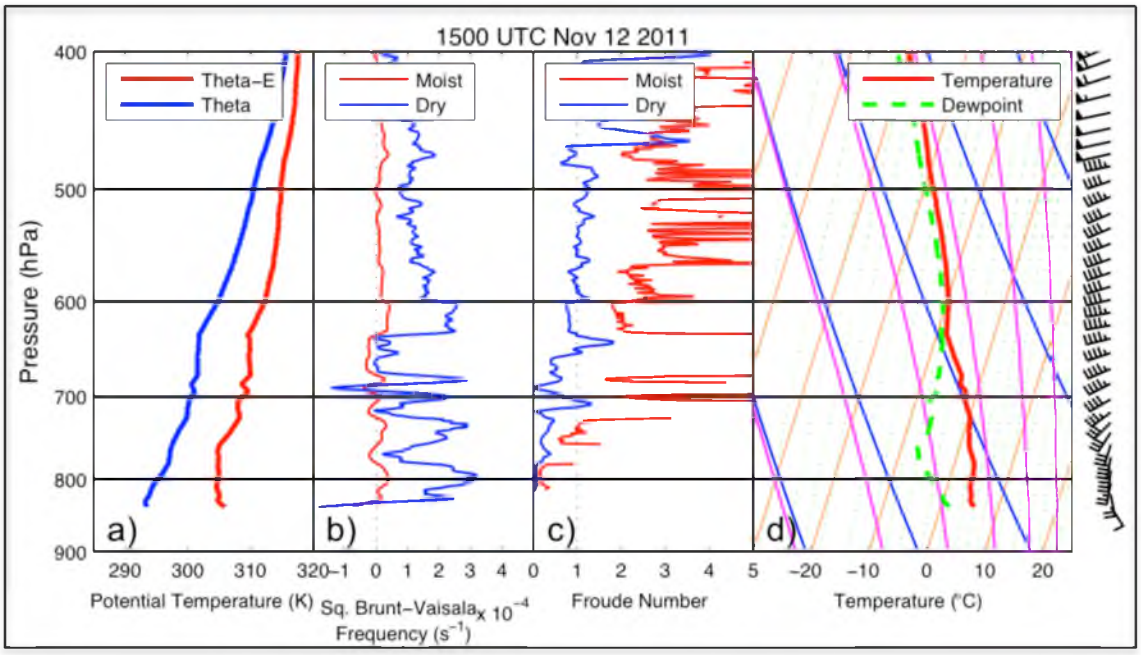

Fig. 6. Upper-air observations for 1500 UTC 12 November at DOW6 site. (a) θ and θ_e. (b) N_d^2 and N_m^2. (c) Dry Froude number and moist Froude number. (d) Skew T-log$p$ diagram [temperature, dewpoint, and wind barbs (full and half barbs denote 5 and 2.5 m s^{-1}, respectively)].

During this period, the KMTX radar showed persistent quasistationary echoes in three areas (Fig. 5d). The first is in the lowlands upstream of the northern Wasatch Mountains where there was an area of windward precipitation enhancement (hereafter the windward precipitation region; region A), as frequently occurs during large-scale southwesterly flow (e.g., Cox et al. 2005). The second is over the central Wasatch Mountains east of the SLV, including upper LCC, where there was a barrier-scale precipitation maximum near the Wasatch Crest (hereafter the barrier-scale precipitation maximum; region B). The third is over the southern SLV where a west–east oriented band of reflectivity returns extended from the Oquirrh Mountains into the central Wasatch Mountains near LCC (hereafter the cross-valley band; region C). The barrier-scale precipitation maximum and the cross-valley band are also present in DOW6 PPI scans (composite time-mean shown later). Although a prominent feature on NEXRAD and DOW6 PPI scans, the cross-valley band produced little measurable precipitation in the SLV, as precipitation sublimated in the dry airmass below crest level (the KMTX radar is located ~700 m above the SLV floor). Photographs taken during this period from the DOW6 site show virga beneath the cross-valley band, with little visual evidence of precipitation reaching the surface (not shown).

The lack of windward precipitation enhancement upstream of the central Wasatch Mountains may reflect the influence of the Stansbury and Oquirrh Mountains to the west (see Fig. 1a for locations). The southern terminus of the windward precipitation region was roughly aligned with the northernmost extent of west–southwest midlevel flow that traversed those barriers (Fig. 5d). Less clear are

the mechanisms for the cross-valley band, which formed east of the Oquirrh Mountains.

The Up-Canyon North RHI scan from 1543 UTC 12 November illustrates the wave-like radar reflectivity structure formed over the SLV and LCC by the cross-valley band and barrier-scale precipitation maximum (Fig. 7). Radar reflectivity returns associated with the cross-valley band descend from west-to-east across the SLV. High reflectivities associated with the wave-like barrier-scale precipitation maximum then ascend, broaden, and strengthen over middle LCC before sloping downward over upper LCC. During this period CLN recorded light precipitation (1.5–3 mm SWE h^{-1}, Fig. 4a) and upper LCC was obscured (not shown).

Time-mean reflectivity RHIs for 1430–1700 UTC 12 November (Fig. 8a–c) show a similar structure over the Cottonwood and Alpine Ridges to the north and south of LCC, respectively. Note the eastward displacement (downstream relative to the midlevel flow) of the reflectivity maximum relative to Twin Peaks and Lone Peak, despite the fact that these peaks form the windward face of the central Wasatch Mountains, rising ~2000 m above the SLV. The composite time-mean reflectivity PPI for 1430–1700 UTC 12 November also shows this displacement (Fig. 8d), with the barrier-scale reflectivity maximum located along the Wasatch Crest and east (downstream) of the initial windward peaks.

The Up-Canyon North time-mean Doppler velocity RHI for 1430–1700 UTC 12 November (Fig. 9a) shows a shallow layer of inbound radial velocities over the SLV, consistent with the southeasterly surface flow (Fig. 5c). This is surmounted by a layer of strong Doppler velocity shear that, like the radar reflectivity maximum,

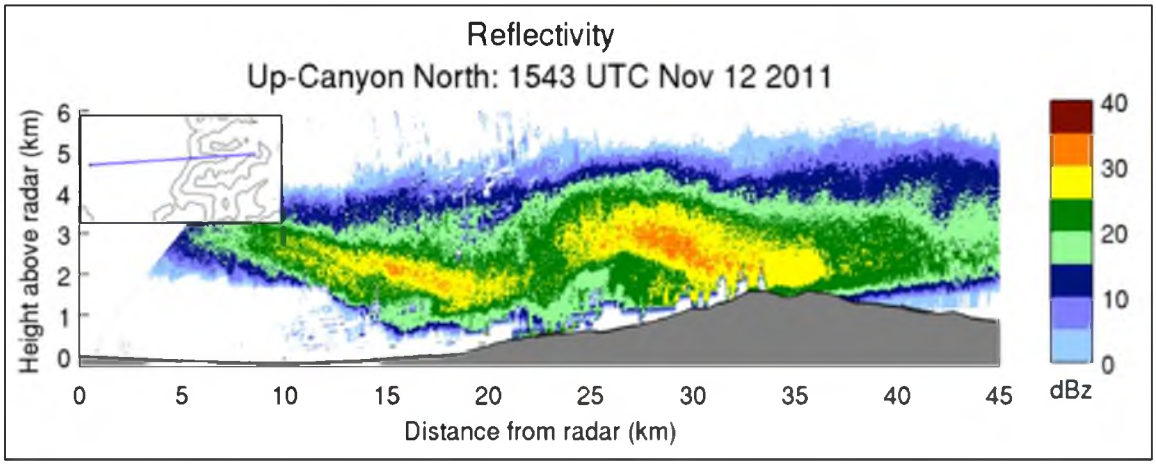

Fig. 7. Radar reflectivity Up-Canyon North RHI scan (dBZ, shaded following scale at right) for 1543 UTC 12 November.

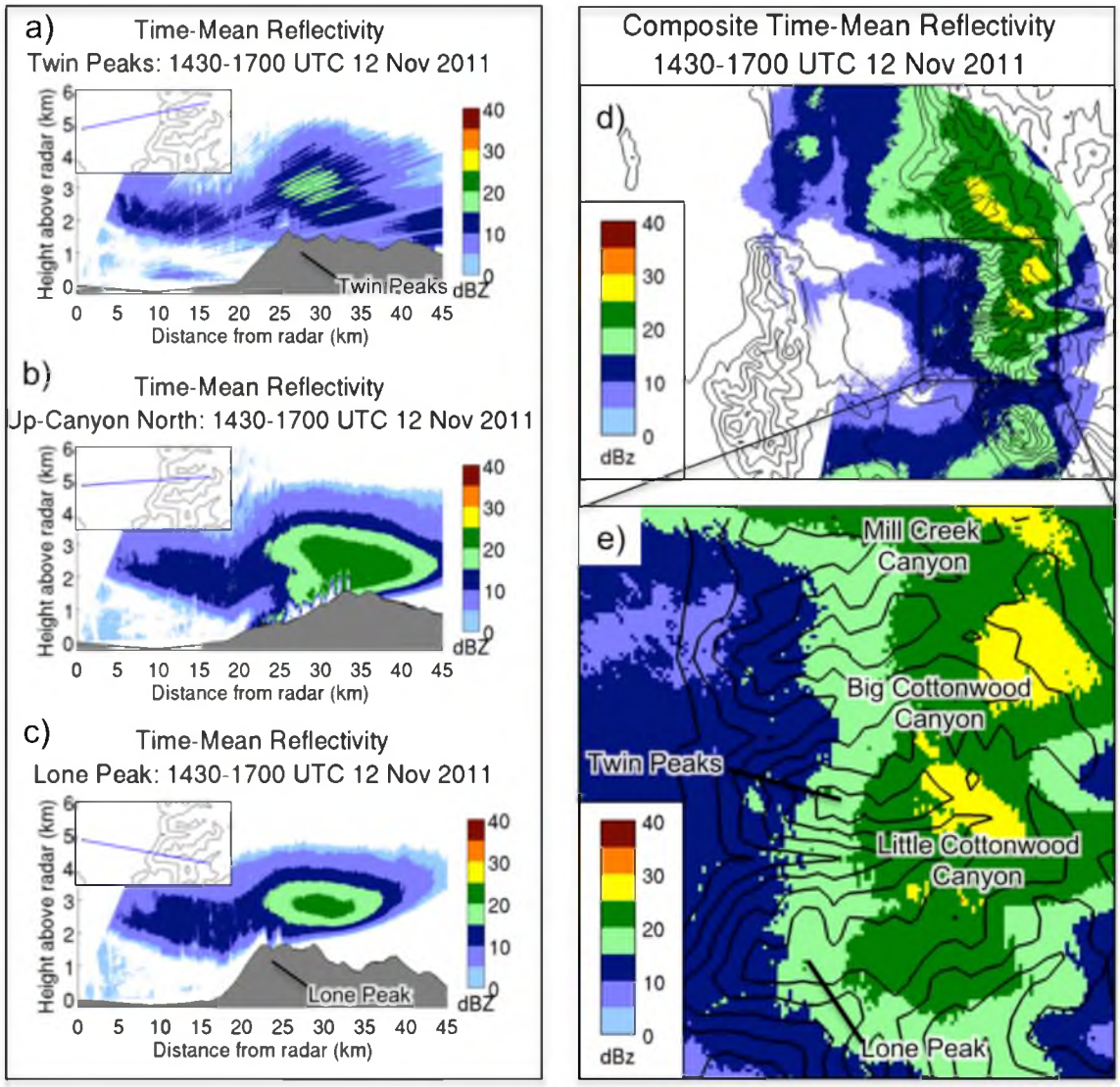

Fig. 8. Time–mean radar reflectivity (dBZ, shaded following scale at right) for 1430–1700 UTC 12 November. (a) Twin Peaks RHI. (b) Up-Canyon North RHI. (c) Lone Peak RHI. Time-mean composite radar reflectivity for 1430–1700 UTC 12 November (dBZ, shaded following scale at lower left) for (d) the SLV region and (e) the central Wasatch Mountains.

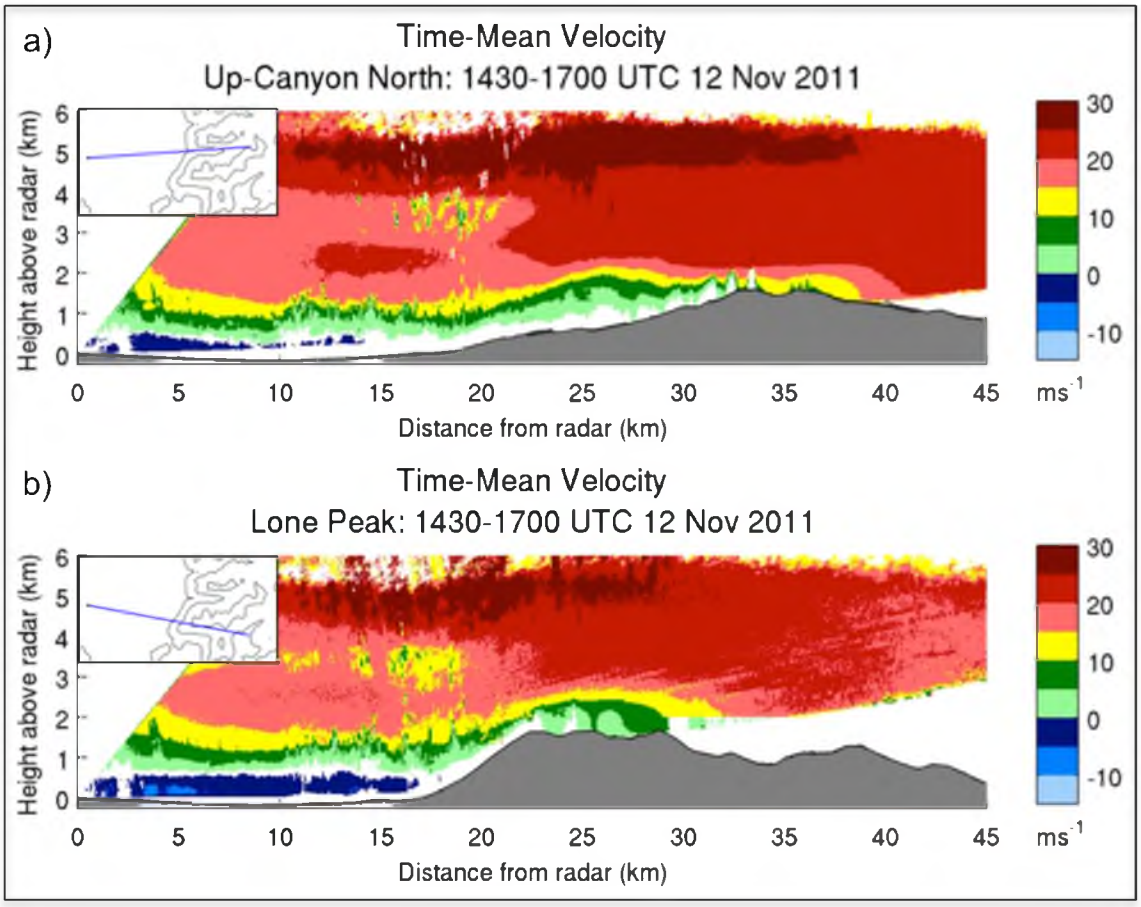

Fig. 9. Time–mean Doppler velocity (m s^{-1}, shaded following scale at right, positive values denote flow away from radar) for 1430–1700 UTC 12 November. (a) Up-Canyon North RHI. (b) Lone Peak RHI.

slopes upward over lower and middle LCC, reaching a maximum height ~26 km from the radar (cf., Fig. 9a and Fig. 8b). The Lone Peak time-mean Doppler velocity RHI for 1430–1700 UTC 12 November shows similar characteristics (Fig. 9b), but with a stronger slope over the western face of Lone Peak leading to a maximum height that is about ~500 m higher than found over LCC (cf. Fig. 9a,b). MesoWest observations from Mt. Baldy (AMB; 3373 m; see Fig. 2a for location) and surrounding sites show strong south–southwesterly flow penetrating across the Alpine Ridge south of LCC during this period (Fig. 5c). This is a stronger and more southerly flow than found at a comparable elevation (~650 hPa) in the 1500 UTC 12 November sounding taken over the SLV (Fig. 6). Thus, beneath the sloping shear layer and inferred cross-barrier ascent that generated the barrier-scale precipitation maximum, south–southwesterly flow was able to surmount the Alpine Ridge and descend over LCC. A similar structure in Twin Peak RHIs (not shown) suggests a shallow wave-like flow across the ridge-canyon corrugations of the central Wasatch Mountains. The 1638 UTC 12 November photograph from the DOW6 site, taken when precipitation over the SLV had abated but a similar structure persisted over the central Wasatch Mountains, shows the shallow orographic cumulus cloud generated by this flow over Lone Peak and Twin Peaks (Fig. 10). Careful inspection of the composite time-mean reflectivity PPI shows a tendency for higher reflectivities to extend westward over the Wildcat, Cottonwood, and Alpine Ridges and retract eastward over Mill Creek Canyon, Big Cottonwood Canyon, and LCC (Fig. 8e). Similar effects have been reported over the Cascade Mountains by Garvert et al. (2007).

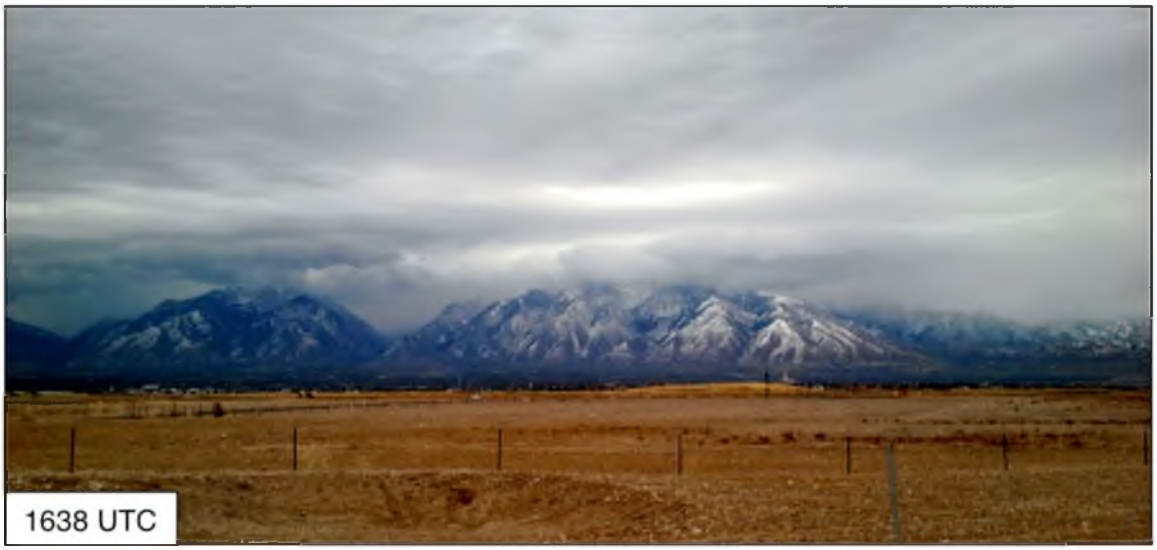

Fig. 10. Photo of prefrontal clouds in and around LCC taken from DOW6 site at 1638 UTC 12 November.

Up-Canyon North hydrometeor type RHIs for 1430–1700 UTC 12 November identify a region of low-density graupel above mid- to upper LCC (25–40 km from the radar; Fig. 11a) that is roughly collocated with the wave-like reflectivity maximum noted in radar reflectivity RHIs (Fig. 7 and Fig. 8a–c). Ice crystals are shown in the higher reaches of the precipitating cloud, while aggregates are shown west (upstream) and east (downstream) of the region of low-density graupel, and the HYVIS camera observed rimed crystals and small graupel in upper LCC during this period (Fig. 11b). Graupel is most likely present in this region due to the increased vertical motion and associated higher cloud liquid water values and residence times over the Wasatch crest.

Between 1700–1900 UTC 12 November the windward precipitation band upstream of the northern Wasatch Mountains dissipated with the approach of the surface-based cold front (not shown). Over and around the SLV, the cross-valley band dissipated, the barrier-scale precipitation maximum persisted in a somewhat weakened state (Fig. 12), and precipitation rates at CLN ebbed (Fig. 4). Although the time-mean Doppler velocity RHIs have gaps in coverage over the valley due to the lack of radar returns throughout much of this period, the velocity signatures above mid- to upper LCC and Lone Peak show that the Doppler velocity shear layer is flatter, no longer exhibiting a wave-like shape (cf. Fig. 9 and Fig. 13). In addition, the hydrometeor type RHI showed aggregates to be the predominant hydrometeor type over the upper canyon, consistent with the observed ice crystal types (Fig. 11c,d). These changes suggest a weakening of precipitation dynamics compared to earlier in IOP6 when precipitation rates, radar reflectivities, riming, and graupel

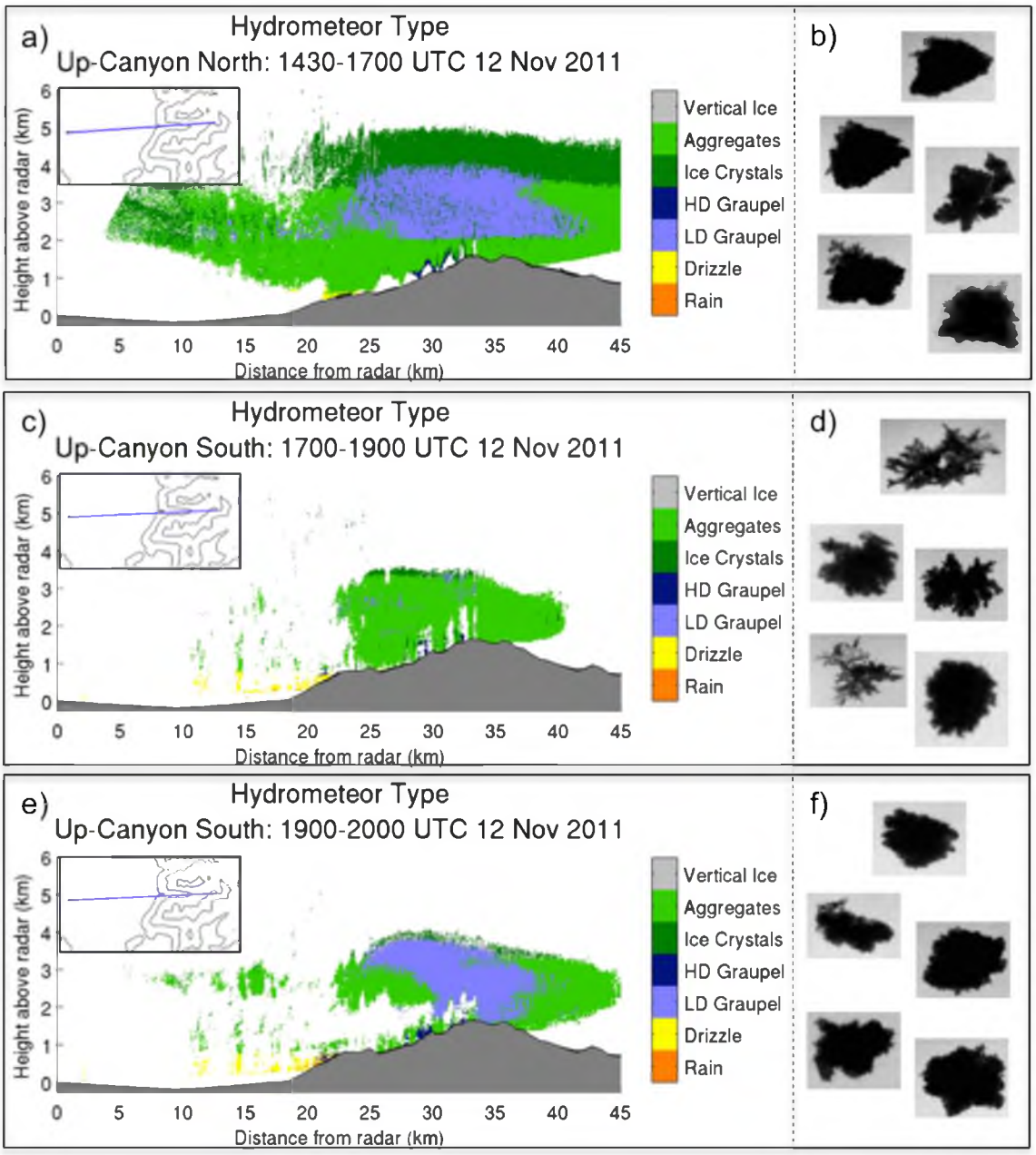

Fig. 11. Hydrometeor type (shading following legend at right where HD and LD refers to high-density and low-density and drizzle refers to drizzle or light rain) and images of snowflakes observed in upper LCC during the same time period. (a,b) Up-Canyon North, 1430–1700 UTC 12 November. (c,d) Up-Canyon South, 1700–1900 UTC 12 November. (e,f) Up-Canyon South, 1900–2000 UTC 12 November.

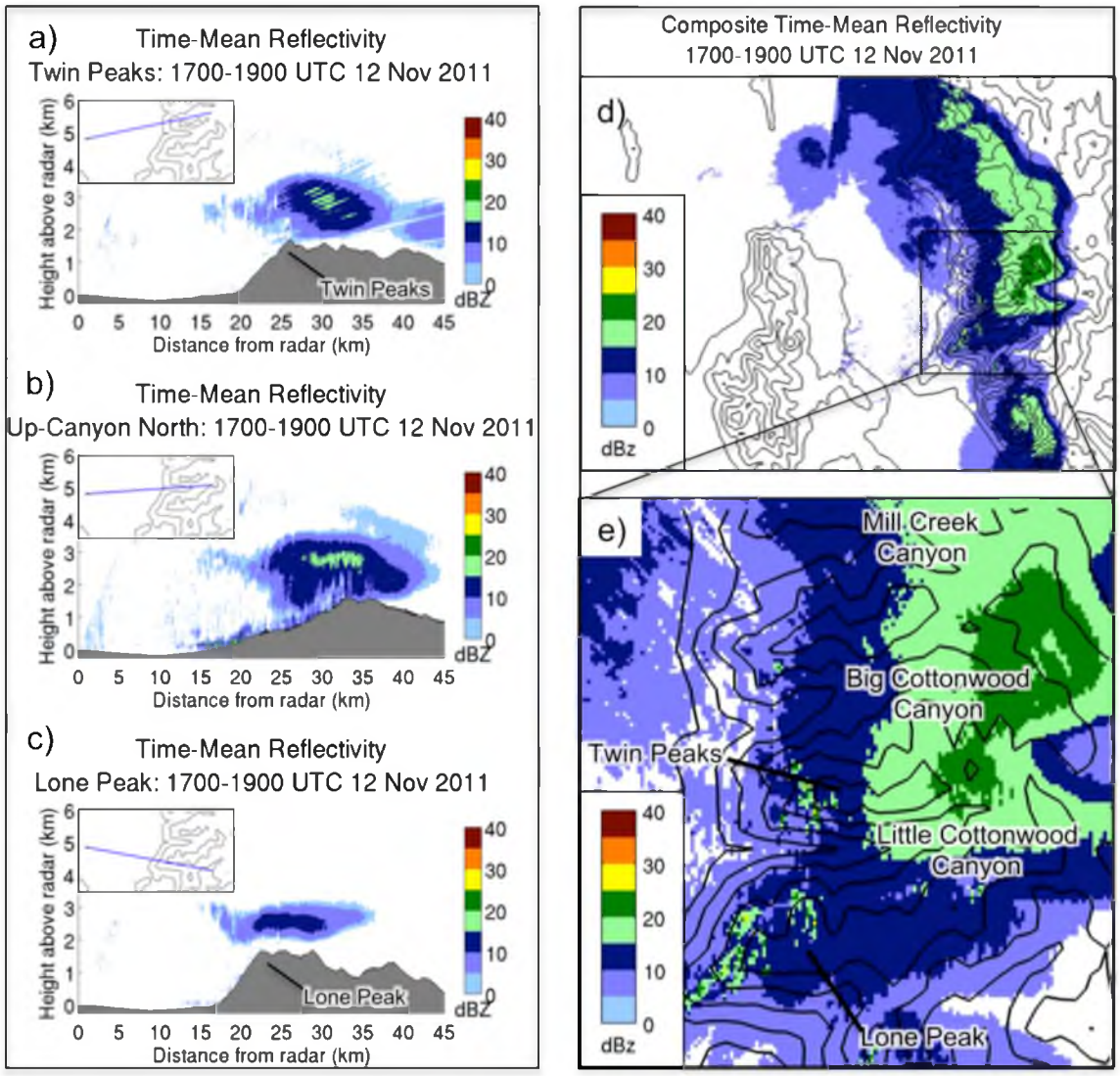

Fig. 12. Time–mean radar reflectivity (dBZ, shaded following scale at right) for 1700–1900 UTC 12 November. (a) Twin Peaks RHI. (b) Up-Canyon North RHI. (c) Lone Peak RHI. Time-mean composite radar reflectivity for 1700–1900 UTC 12 November (dBZ, shaded following scale at lower left) for (d) the SLV region and (e) the central Wasatch Mountains.

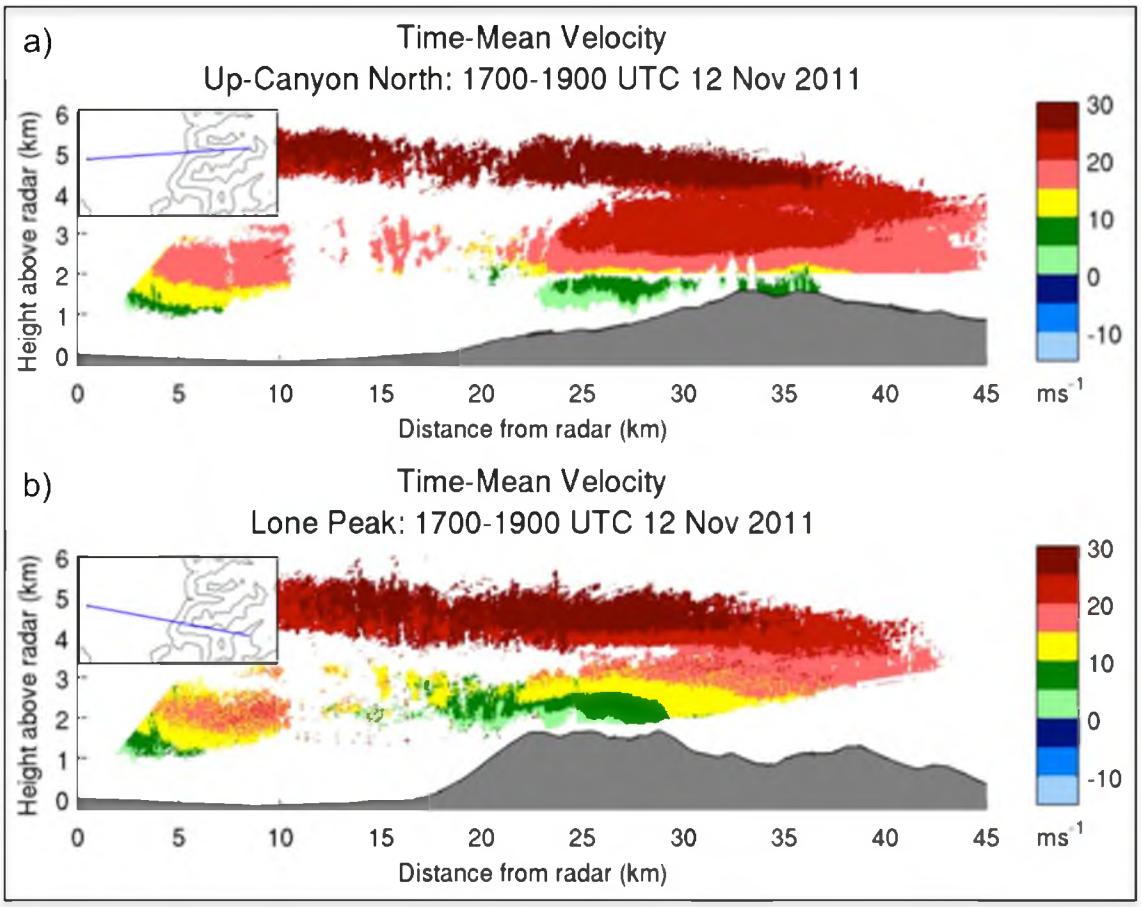

Fig. 13. Time–mean Doppler velocity (m s^{-1}, shaded following scale at right, positive values denote flow away from radar) for 1700–1900 UTC 12 November. (a) Up-Canyon North RHI. (b) Lone Peak RHI.

content were all greater. This is broadly consistent with weaker large-scale ascent and lower surface–725-hPa relative humidities in the RUC2 analysis at 1800 UTC 12 November (Fig. 3) and the inferred weakening of the wave-like structure in radar reflectivity and Doppler velocity shear. This was also reflected by the predominance of aggregates in upper LCC when the wave-like structure weakened, while graupel and heavily rimed crystals were observed when the wave-like structure was stronger. This includes a second, shorter period between 1900–2000 UTC, when the wave-like feature was again observed and hydrometeor type RHIs show a region of low-density graupel above upper LCC (Fig. 11e,f). These contrasts suggest that the increase in vertical motion from multiscale wave-like undulations increased the available cloud liquid water, residence times, and resultant riming over LCC, similar to that found by Bruintjes et al. (1994) in a winter storm over Arizona.

Frontal Stage

At 2000 UTC 12 November, the surface-based cold front was moving through the SLV (wind shift visible in Fig. 14c) with the 700-hPa baroclinic zone and 500-hPa trough axis just upstream (Fig. 14a,b). Just after frontal passage, at 2030 UTC 12 November, a sounding launched from the DOW6 site (Fig. 15) showed shallow northwesterly flow with two apparent frontal stable layers between 825 and 775 hPa.

The shallow surface-based cold front was distorted by the Oquirrh and Wasatch Mountains as it progressed into the SLV, but was much weaker at upper

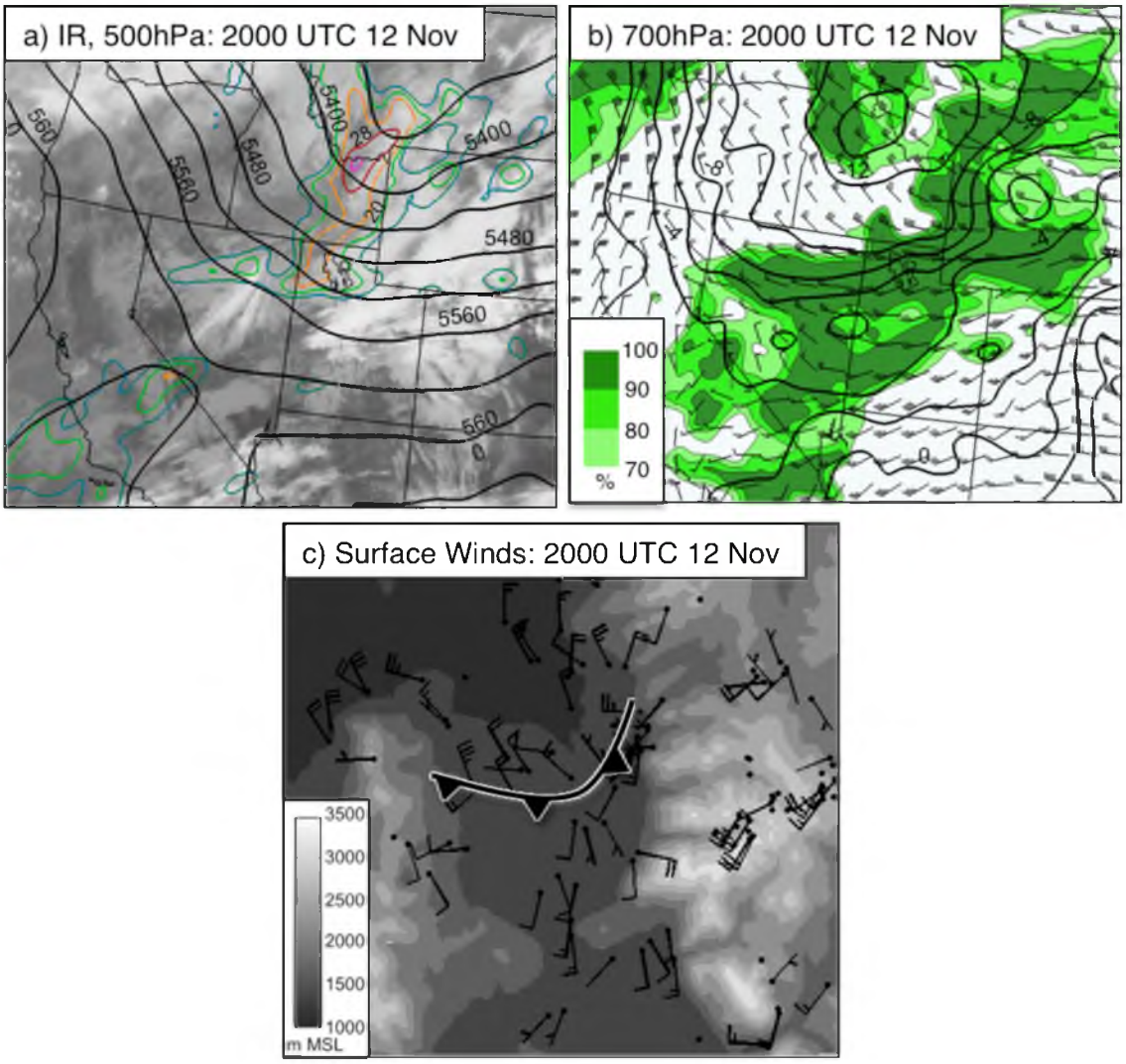

Fig. 14. Environmental conditions for 2000 UTC 12 November. (a) RUC2 500-hPa geopotential height (black contours every 60 m) and absolute vorticity (colored contours every $4x10^{-5}$ s^{-1}), and infrared satellite image. (b) RUC2 700-hPa temperature (black contours every 2°C), wind (full and half barbs denote 5 and 2.5 m s^{-1}, respectively), and relative humidity (%, shaded following scale at lower left). (c) MesoWest wind surface observations [wind barbs as in (b)] and terrain elevation (m, shaded following scale at lower left) with manual surface front analysis (heavy black line).

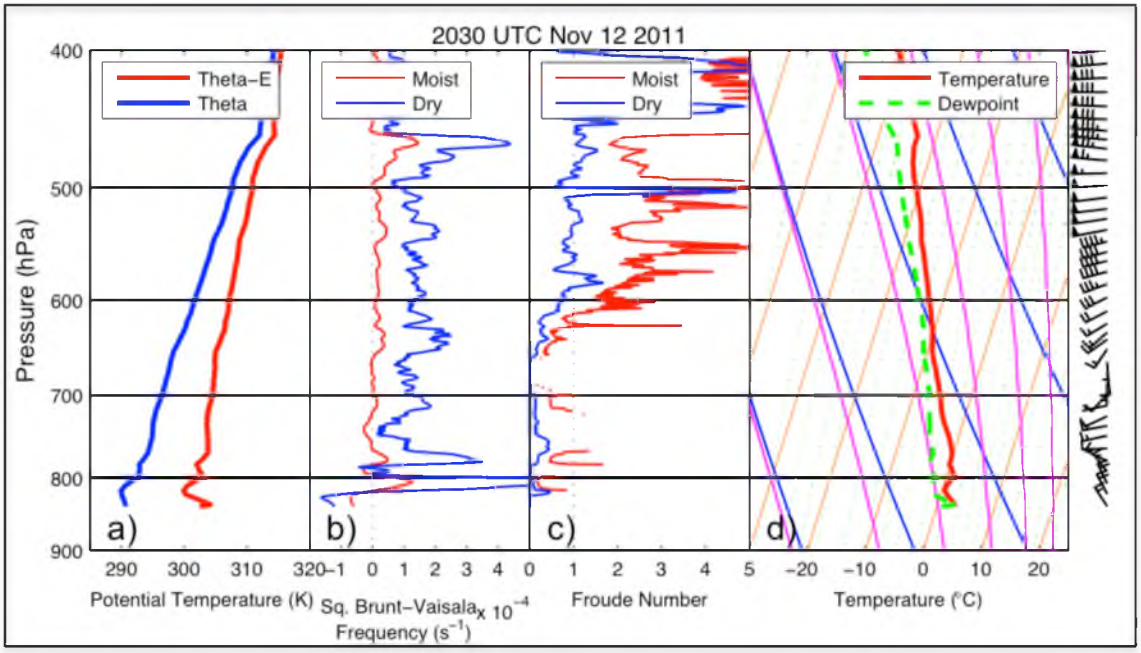

Fig. 15. Upper-air observations for 2030 UTC 12 November at DOW6 site. (a) θ and θ_e. (b) N_d^2 and N_m^2. (c) Dry Froude number and moist Froude number. (d) Skew T-log$p$ diagram [temperature, dewpoint, and wind barbs (full and half barbs denote 5 and 2.5 m s^{-1}, respectively)].

elevations (Fig. 16a, 2002 UTC 12 November, front analyzed at lower elevations where it was well defined). For example, a gradual wind shift (SSW to WSW) and small (1° C) temperature decline were observed at AMB, while a more dramatic wind shift (S to N) and large (10° C) temperature decline were observed at KSLC. A band of precipitation ~30-km wide (hereafter the frontal band) accompanied the cold front, and its presence is used in this thesis to define the frontal stages at KSLC (1940–2100 UTC 12 November) and LCC (2025–2130 UTC 12 November). As the frontal band moved through the SLV, it was strongly modulated by the terrain with enhancement on the western slopes of the Oquirrh Mountains, shadowing over the western SLV, and enhancement again over the western slopes of the Wasatch Mountains. By 2030 UTC 12 November (Fig. 16b), the front had penetrated to the south end of the SLV and was draped across lower LCC. Enhancement of the frontal band continued over the Oquirrh and Wasatch Mountains while the western SLV remained shadowed. By 2100 UTC 12 November (Fig. 16c), the cold front was south of the SLV and LCC and precipitation was confined to very near and over the Wasatch Mountains. At the same time, a broader area of postfrontal precipitation (Fig. 16b,c; hereafter the postfrontal band) had stalled at the northern end of the SLV.

Up-Canyon South radar reflectivity RHIs between 2026 and 2052 UTC 12 November document the precipitation structure in and around LCC during frontal passage (Fig. 17). As the canyon is oriented roughly west–east and the cold front was oriented southwest–northeast, these RHIs cut obliquely through the front. At

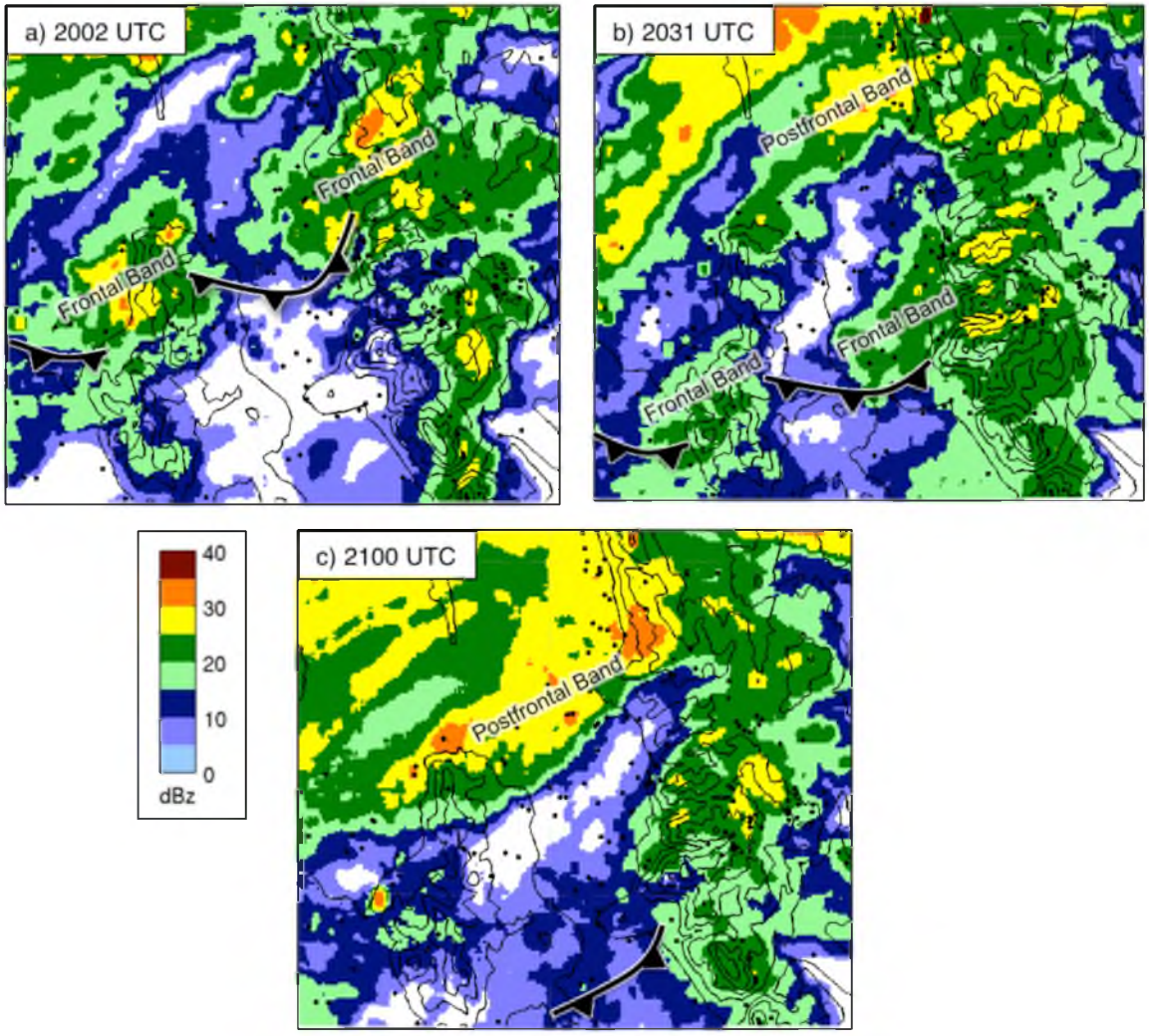

Fig. 16. KMTX lowest-elevation angle (0.5°) base reflectivity (shaded following scale at lower left) and manual surface-front analysis (heavy black line) for (a) 2002 UTC 12 November, (b) 2031 UTC 12 November, and (c) 2100 UTC 12 November. Black dots mark the locations of mesonet stations used in the analysis of the surface-front boundary.

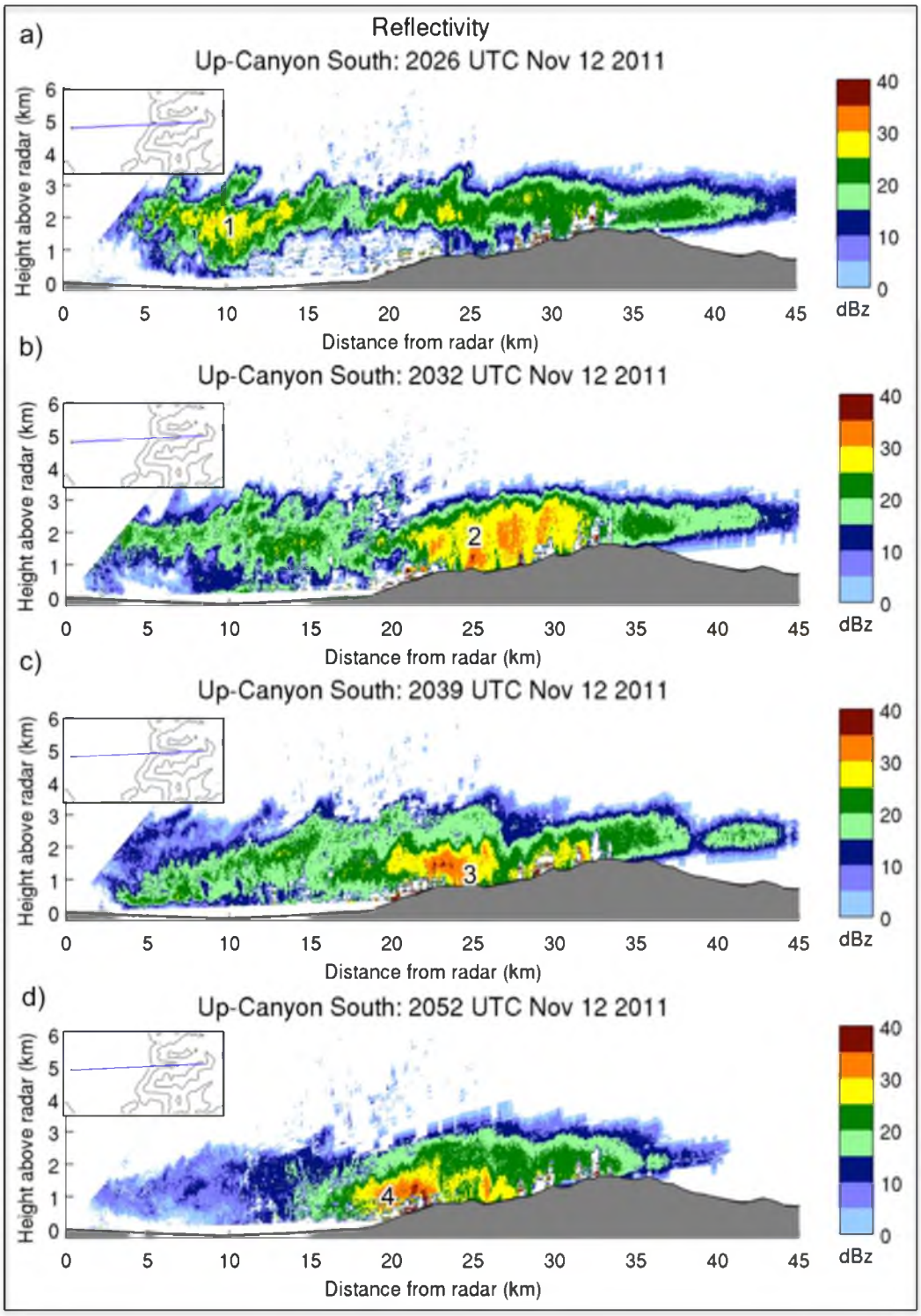

Fig. 17. Up-Canyon South radar reflectivity RHI scans (dBZ, shaded following scale at right) for (a) 2026 UTC 12 November, (b) 2032 UTC 12 November, (c) 2039 UTC 12 November, and (d) 2052 UTC 12 November.

2026 UTC 12 November (Fig. 17a), the RHI slices through the frontal band ~10 km from the radar where there is an elevated region of 20–30 dBZ reflectivities (labeled area 1). Lower reflectivities below this maximum suggest the sublimation of hydrometeors in the subsaturated air below crest level (Fig. 15), and a photograph taken at 1957 UTC 12 November from the DOW6 site (looking towards the west face of the central Wasatch Mountains, Fig. 18) shows the sublimation of precipitation behind the fractus cloud at the leading edge of the cold front. By 2032 UTC 12 November (Fig. 17b), the frontal band had moved across the Cottonwood ridge and into LCC, increasing radar reflectivities within the midcanyon (area 2). This area of high reflectivities became shallower by 2039 UTC 12 November (Fig. 17c; area 3) and gradually became concentrated in the lower canyon (Fig. 17d; area 4). After passage of the frontal band, radar reflectivities diminished significantly and became quite shallow in and around LCC. The lower canyon, however, maintained a small reflectivity maximum averaging 15–20 dBZ until ~2130 UTC 12 November (not shown).

Between 2025–2100 UTC 12 November time-mean reflectivity RHIs show a relatively deep region of frontal precipitation within LCC, with the strongest reflectivities over the midcanyon (Fig. 19b). Time-mean reflectivities over the Cottonwood and Alpine Ridges to the north and south did not reach a comparable depth or intensity as that within the canyon during this period (Fig. 19a,c). These marked contrasts are also visible in the composite time-mean reflectivity PPI scan for the period (Fig. 19d,e), which shows the highest radar reflectivities within lower LCC as well as over the north- to northwest-facing walls of lower Mill Creek Canyon,

Fig. 18. Photograph of surface-based cold front looking northeast from the DOW6 site. Note the fractus cloud above the leading edge of the cold front, and the sublimation behind it.

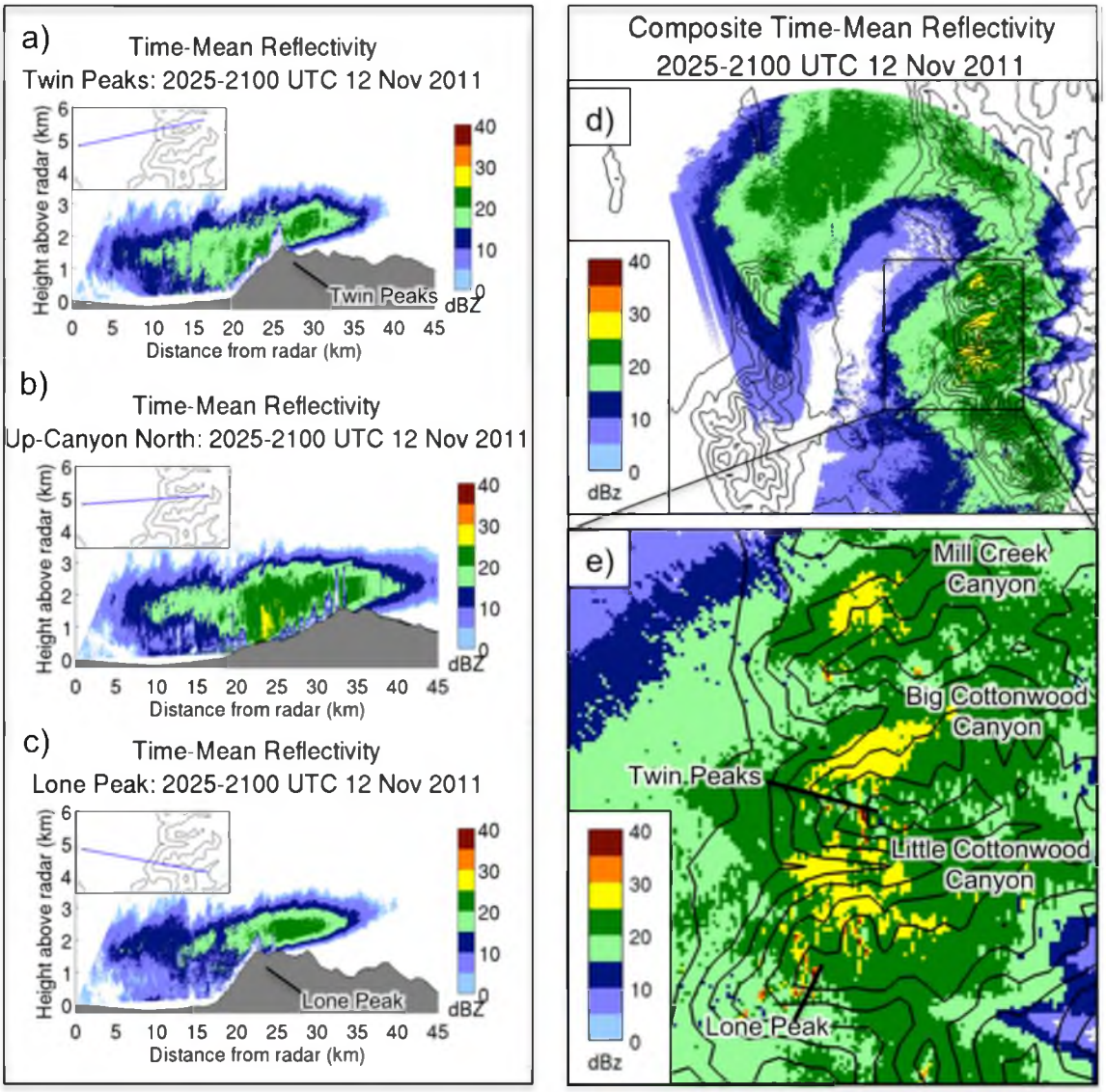

Fig. 19. Time–mean radar reflectivity (dBZ, shaded following scale at right) for 2025–2100 UTC 12 November. (a) Twin Peaks RHI. (b) Up-Canyon North RHI. (c) Lone Peak RHI. Time-mean composite radar reflectivity for 2025–2100 UTC 12 November (dBZ, shaded following scale at lower left) for (d) the SLV region and (e) the central Wasatch Mountains.

Big Cottonwood Canyon, and LCC. Reflectivities were lower at high elevations along the Wildcat, Cottonwood, and Alpine Ridges, implying that the storm during this period was relatively shallow with localized, northwesterly upslope flow immediately behind the front creating orographic enhancement at midelevations along the north- to northwest-facing canyon walls.

As the cold front progressed through LCC the hydrometeor type RHI for 2025–2100 UTC 12 November (Fig. 20a) shows a layer of low-density graupel extending over LCC and the SLV with a shallow layer of aggregates in the low-levels above the SLV. The vigorous vertical motion often associated with frontal precipitation would result in increased riming, and the observation of small graupel and heavily rimed crystals over upper LCC (Fig. 20b) confirms the hydrometeor classification at higher elevations. There is no way to confirm the actual hydrometeor types over the SLV at this time because of sublimation and a lack of snow crystal identification observations in the SLV, however, it is unlikely that a precipitating cloud would be composed of such a broad layer of aggregates below a layer of graupel. This suggests either a misclassification of the predominant hydrometeor type over the SLV by the Dolan and Rutledge (2009) algorithm or a shift in the actual hydrometeor types over the SLV during the passage of the frontal precipitation band. Notably, Houze and Medina (2005) found a similar misclassification between large aggregates and graupel using the hydrometeor typing algorithm by Vivekanandan et al. (1999).

The Dolan and Rutledge (2009) algorithm includes many overlaps in the ranges used for low-density graupel and aggregates due to their similar sizes, axis

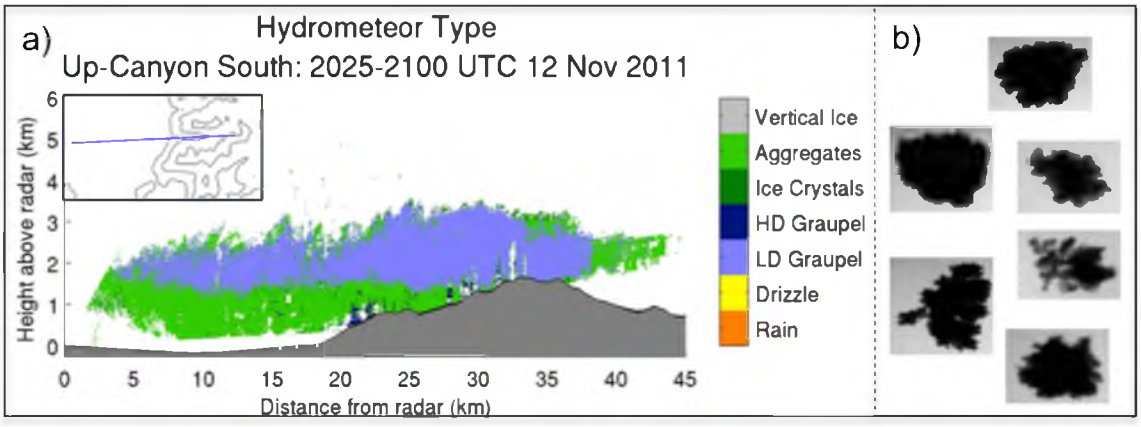

Fig. 20. Up-Canyon South hydrometeor type (shading following legend at right where HD and LD refers to high-density and low-density and drizzle refers to drizzle or light rain) and images of snowflakes observed in upper LCC for 2025–2100 UTC 12 November.

ratios and temperature ranges. Due to these similarities, the misclassification may stem from either reflectivity or temperature variations along the RHI or possibly the lack of specific differential phase in our use of the algorithm (discussed in Data and Methods). The region of low-density graupel does not appear to retain the shape of the highest reflectivities seen on time-mean RHIs (cf. Fig. 19, Fig. 20), instead exhibiting an abrupt elevational transition to aggregates, which suggests that reflectivity is not the culprit. Given that one temperature profile (from a sounding launched on the west side of the SLV) was extrapolated across the RHI for the entire frontal stage, it is likely that the large temporal and spatial temperature variations below crest level over the SLV and LCC during passage of the shallow cold front were not sufficiently represented by the sounding. This leads us to believe that an inaccurate temperature profile was the primary cause of the misclassification.

The spatial contrasts in reflectivity patterns between 1430–1700 UTC 12 November (Fig. 8) and 2025–2100 UTC 12 November (Fig. 19) are striking. Between 1430–1700 UTC 12 November the composite time-mean reflectivity PPI (Fig. 8d,e) shows that the reflectivity maxima were located along the Wasatch Crest, eastward (downstream in the midlevel flow) of the high peaks, and that there was a tendency for higher reflectivities to extend westward along the transverse ridges. Time-mean reflectivity RHIs (Fig. 8a–c) show that the reflectivity maxima were lifted above upper LCC and the eastern Cottonwood and Alpine Ridges. The composite time-mean reflectivity for PPI 2025–2100 UTC 12 November, however, indicated a near reversal of the spatial pattern described above during the frontal stage. The reflectivity maxima were found over lower LCC and at midelevations along the

north- to northwest- facing walls of Mill Creek Canyon, Big Cottonwood Canyon, and time-mean reflectivity RHIs show that these maxima hugged the surface of the canyon rather than appearing lifted above the barrier.

Postfrontal Stage

At 0000 UTC 13 November, about halfway through the postfrontal stage, the 500-hPa trough and vorticity maximum were aligned over northern Utah and 700-hPa winds were west-northwesterly behind the 700-hPa baroclinic zone (Fig. 21a,b). The 0000 UTC 13 November KSLC sounding (Fig. 22) showed a postfrontal atmosphere featuring a layer between 650–550 hPa that was saturated and moist neutral with near constant θ_e, while below crest level (~700 hPa) large N_d^2 and N_m^2 and low dry Froude numbers (<1) favored low-level blocking. Surface winds at 0000 UTC 13 November had shifted from northerly to predominantly easterly and light (Fig. 21c), and midlevel winds were predominantly westerly, veering to northwesterly aloft (Fig. 22).

KMTX NEXRAD radar reflectivity scans from 2031 and 2100 UTC 12 November (Fig. 16b,c) show the postfrontal precipitation band stalled at the northern end of the SLV, where it persisted until around 2200 UTC 12 November, bringing KSLC its first bout of measureable precipitation while much of the SLV remained dry (Fig. 4). LCC and the southern end of the SLV received only sporadic and very light precipitation as shear-parallel convective bands organized in the increasingly convective precipitation that filled northern half of the SLV between

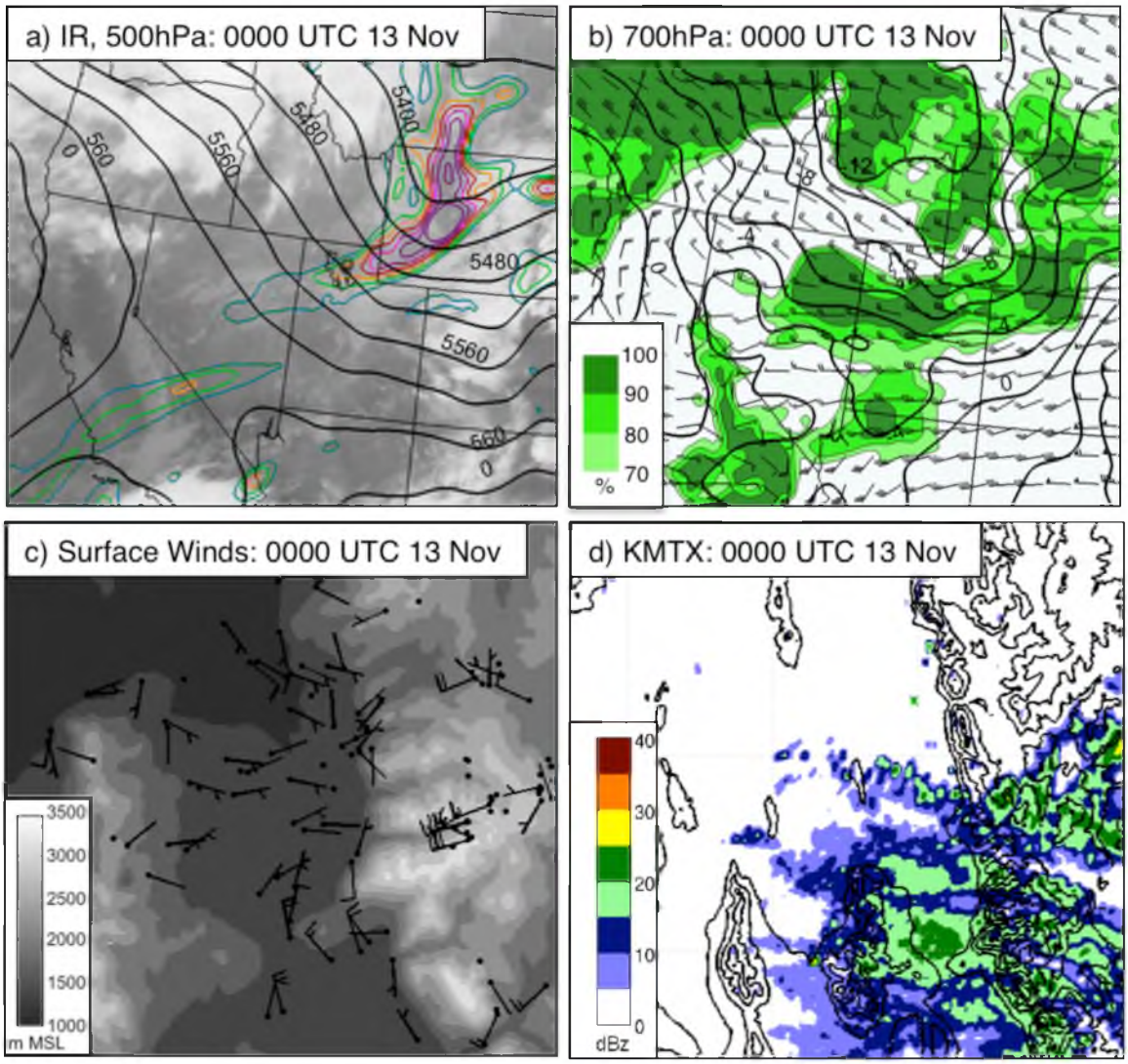

Fig. 21. Environmental conditions for 0000 UTC 13 November. (a) RUC2 500-hPa geopotential height (black contours every 60 m) and absolute vorticity (colored contours every 4×10^{-5} s^{-1}), and infrared satellite image. (b) RUC2 700-hPa temperature (black contours every 2°C), wind (full and half barbs denote 5 and 2.5 m s^{-1}, respectively), and relative humidity (%, shaded following scale at lower left). (c) MesoWest wind surface observations [wind barbs as in (b)] and terrain elevation (m, shaded following scale at lower left). (d) KMTX lowest-elevation angle (0.5°) base reflectivity (shaded following scale at lower left).

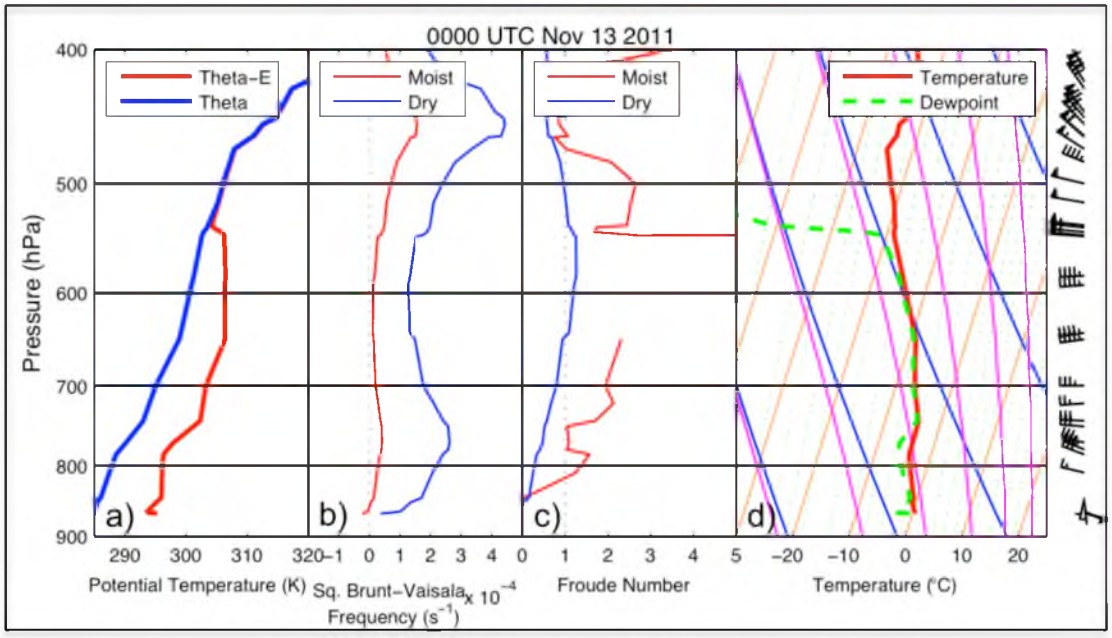

Fig. 22. Upper-air observations for 0000 UTC 13 November at KSLC (launched ~2315 UTC). (a) θ and θ_e. (b) N_d^2 and N_m^2. (c) Dry Froude number and moist Froude number. (d) Skew T-log$p$ diagram [temperature, dewpoint, and wind barbs (full and half barbs denote 5 and 2.5 m s^{-1}, respectively)].

2200–2300 UTC 12 November (not shown), bringing continued heavier precipitation to KSLC.

After ~2300 UTC 12 November transient and scattered shallow convective generating cells filled in over the southern SLV and the central Wasatch Mountains, persisting through 0400 UTC 13 November, the end of IOP6. An example of the precipitation features observed during this period is shown in the composite radar reflectivity PPI for 0030–0035 13 November (Fig. 23) and the Up-Canyon South radar reflectivity and Doppler velocity RHIs from 0032 UTC 13 November (Fig. 24). These figures show shallow generating cells forming just above the layer of strongest wind shear in the saturated moist neutral layer between 650–550 hPa (Fig. 22), with fallstreaks evident below. The cells appear to strengthen and widen slightly as they ascend the higher terrain, but there was no spatial gradient in time-mean radar reflectivity between ridge and canyon locations. Aggregates were observed in upper LCC from 2130–0300 UTC 12–13 November, and the time-mean hydrometeor type RHI shows a layer of ice crystals at the level of the generating cells with a deep layer of aggregates below (Fig. 25), suggesting that ice crystals formed in the weak updrafts of the small convective cells, producing aggregates as they became entangled with other crystals in the lower levels.

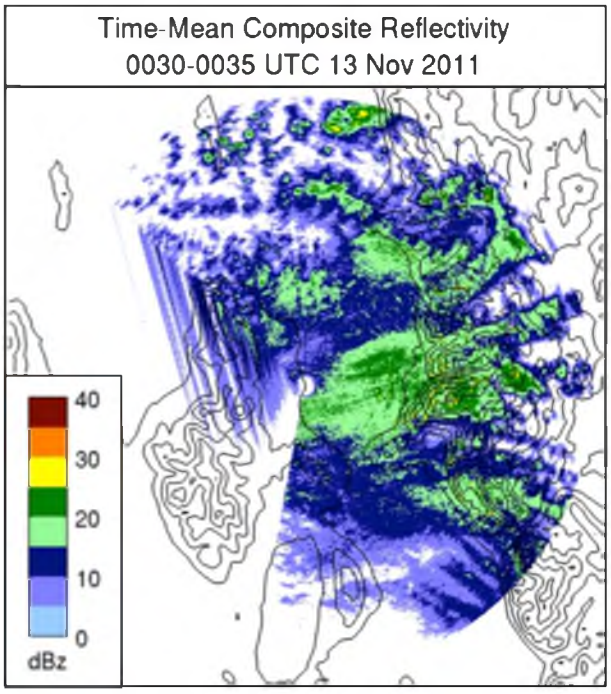

Fig. 23. Composite radar reflectivity for 0030–0035 UTC 13 November (dBZ, shaded following scale at left).

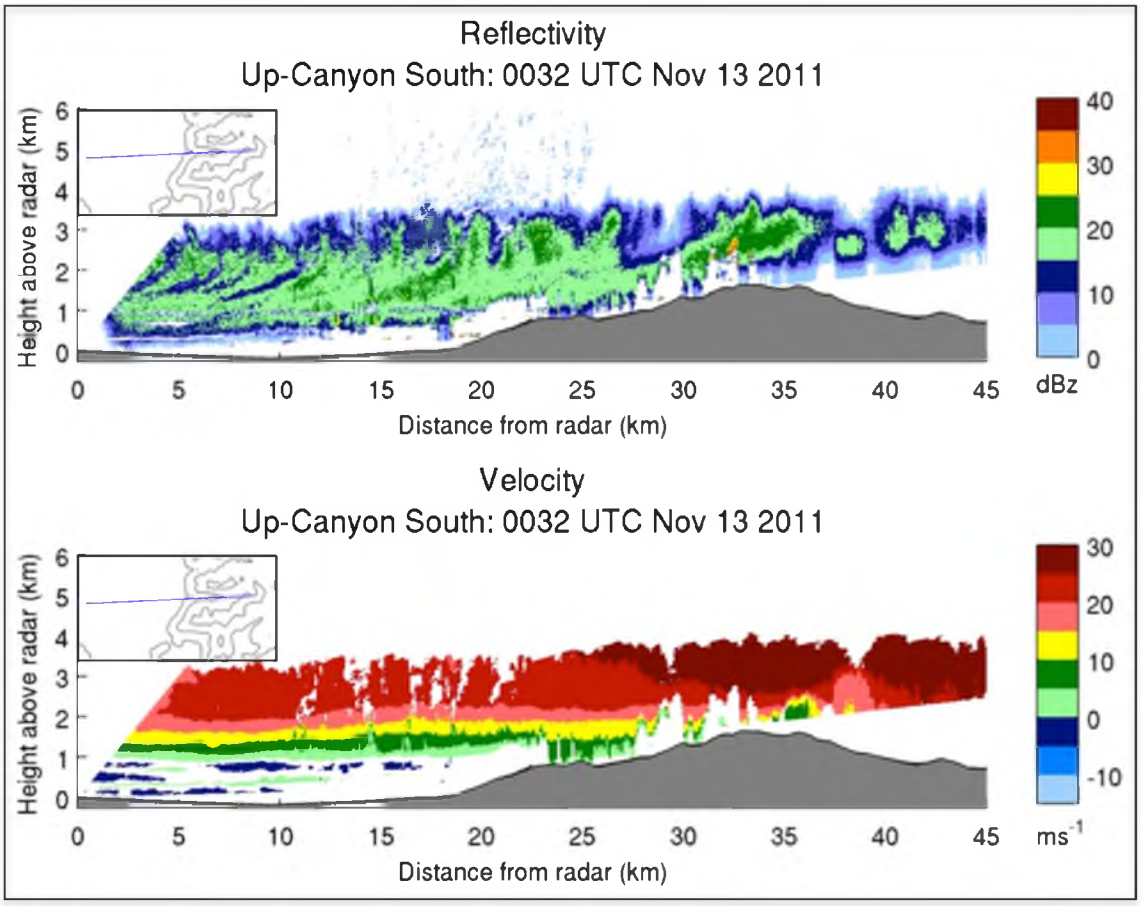

Fig. 24. Up-Canyon South for 1543 UTC 12 November (a) radar reflectivity (dBZ, shaded following scale at right) and (b) Doppler velocity (m s^{-1}, shaded following scale at right).

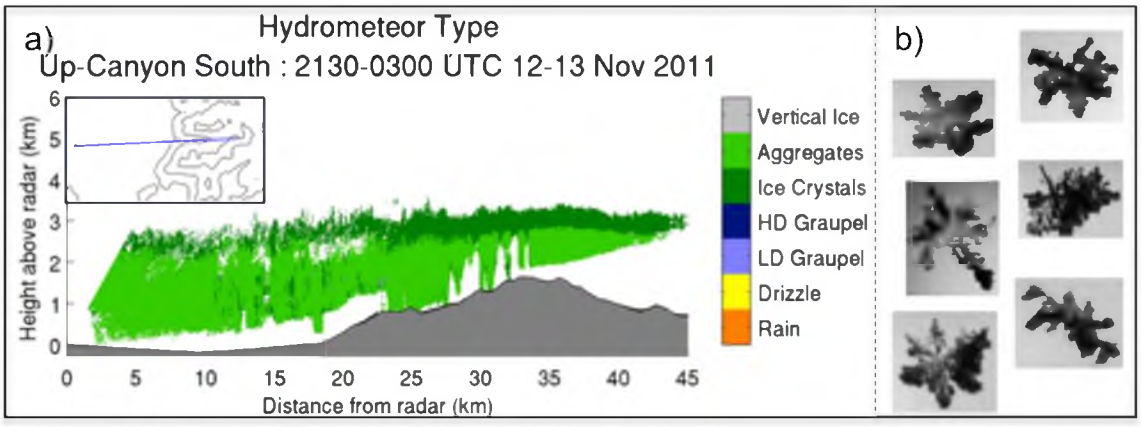

Fig. 25. Up-Canyon South hydrometeor type (shading following legend at right where HD and LD refers to high-density and low-density and drizzle refers to drizzle or light rain) and images of snowflakes observed in upper LCC for 2130–0300 UTC 12–13 November.

CHAPTER 4

DISCUSSION AND CONCLUSIONS

This thesis explores the fine-scale spatiotemporal variability of orographic precipitation structures observed during IOP6 (November 12-13 2011) of the Storm Chasing Utah Style Study (SCHUSS) across the Wasatch Mountains of northern Utah. The use of a ground-based dual-polarization X-band Doppler radar (DOW6) allowed for detailed, fine-scale observations of orographic precipitation in and around Little Cottonwood Canyon (LCC), a deep, glacially carved canyon running orthogonally eastward from the Salt Lake Valley (SLV) into the high terrain of the Wasatch Mountains. IOP6 featured the passage of a progressive upper-level shortwave trough and associated surface-based cold front across the SLV and LCC. Variations in stability and orographic modulation of the synoptic-scale flow created dramatic spatial and temporal gradients in radar reflectivity and structure during the prefrontal, frontal, and postfrontal storm stages.

Persistent quasistationary radar reflectivity features were observed during the stable prefrontal stage in and around LCC and the SLV, including: (1) a barrier-scale precipitation maximum which was found over the Wasatch Crest, east (downstream relative to the midlevel flow) of the high windward peaks; (2) protrusions of higher reflectivity over the transverse ridges flanking LCC and the neighboring canyons; and (3) a cross-valley band of precipitation that extended

from the Oquirrh Mountains across the SLV and into the central Wasatch Mountains. RHI scans through these features revealed a wave-like radar reflectivity structure that sloped downward from west to east across the SLV (cross-valley band), while high reflectivities associated with the barrier-scale precipitation maximum ascended, broadened, and strengthened over middle LCC and then sloped downward over upper LCC. A layer of Doppler velocity shear below this wave-like feature revealed southwest flow that surmounted the Alpine Ridge to the south, descended into LCC, and ascended over the Cottonwood Ridge to the north, appearing to create shallow wave-like flow across the ridge-canyon corrugations of the central Wasatch Mountains. The synergy of the multiscale wave-like features appeared to affect the location and undulating shape of the barrier-scale reflectivity maximum, while low-density graupel was roughly collocated with the reflectivity maxima in RHIs across LCC and the flanking ridges. Figure 26 shows an idealized conceptual model of the wind fields in and around the SLV during this stage.

The terrain encircling the SLV modulated the frontal precipitation band trailing the shallow cold front, with enhancement over the western slopes of the Oquirrh Mountains and central Wasatch Mountains and shadowing in the lee of the Oquirrh Mountains over the western SLV. As the front crossed the central Wasatch Mountains, the depth of the radar reflectivity echoes above the high ridges was relatively shallow, while deeper and more intense radar reflectivities were observed in mid- to lower LCC. This resulted in a radar reflectivity pattern with reflectivity maxima within lower LCC and over the north- to northwest-facing walls of lower LCC and the neighboring canyons and with weaker reflectivities over the transverse

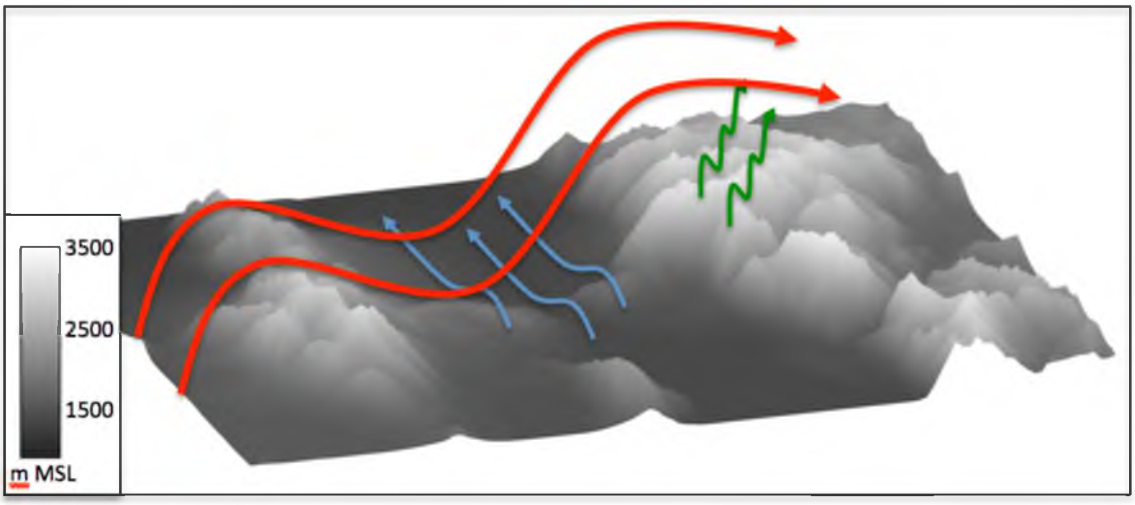

Fig. 26. Three-dimensional idealized schematic diagram of wind flow in and around the SLV for 1430–1700 UTC 12 November.

ridges. While the causes of this pattern could not be fully elucidated with the available data, the shallow nature of both the front and the associated northwest flow might have favored heavier precipitation in the lower canyon rather than over the high terrain and resulted in orographic enhancement along the north- to northwest-facing canyon walls. As frontal precipitation diminished over LCC, the wider, synoptically forced postfrontal precipitation band stalled at the northern end of the SLV, bringing increased precipitation to KSLC early in the postfrontal stage. LCC and the southern end of the SLV received more precipitation later as transient and scattered shallow convective generating cells moved through the SLV, strengthening and widening as they moved above the higher terrain.

While studies such as Frei and Schär (1998), Anders et al. (2007), and Minder et al. (2008) have addressed the problem of small-scale (~10 km) horizontal gradients in precipitation across ridge-valley corrugations over climatological time-scales, fewer studies have examined these processes over hourly or minute time-scales (e.g., Molinié et al. 2012). The present study illustrates how dramatic fine-scale spatiotemporal precipitation features and gradients that do not follow climatological norms can develop within complex terrain such as LCC during the stages of a winter storm. Such departures from climatological norms are especially challenging for forecasting given that: (1) they are poorly observed by existing radar systems, making situational awareness and nowcasting difficult, (2) downscaling of coarse-resolution model guidance is typically done using climatological precipitation–altitude relationships, and (3) current operational numerical modeling systems are unable to explicitly resolve such local effects.

Gradients in precipitation intensity during winter storms have significant implications in heavily used mountainous areas such as LCC, where public safety efforts such as avalanche forecasting and winter road maintenance rely on accurate high-resolution forecasts. State Route 210 (SR-210) follows the north side of LCC from the SLV to its terminus and is traveled by an average of more than 7,000 vehicles each day during winter. Thirty-one avalanche paths bisect the highway, whose steep grade and tortuous path frequently leads to hazardous driving conditions and bumper-to-bumper traffic during winter storms. The number, size, and frequency of avalanches, combined with the volume and speed of traffic, gives SR-210 one of the highest avalanche hazard indices in North America (Little Cottonwood Canyon SR-210 Transportation Study, 2006).

Avalanche hazard during a storm is greatly affected by the intensity and amount of new precipitation, as well as by the temporal and spatial patterns of snow crystal type. The application of a gap-filling X-band radar within LCC would allow for the observation of precipitation features in and around LCC and for the application of hydrometeor typing in real-time during storms, potentially allowing weather forecasters, avalanche professionals, and road maintenance workers to make accurate and well-informed decisions about avalanche hazard and road conditions, with benefits for public safety and Utah's tourist economy.

The utility of X-band radar to fill gaps in radar coverage over mountainous terrain has been noted in the European Alps, where networks of X-band radars are currently being implemented (e.g., Allegretti et al. 2012), and has been considered in mountainous regions within the United States (e.g., Gourley et al. 2009). This thesis

has demonstrated the feasibility and utility of using X-band Doppler radar within LCC to provide high-resolution reflectivity observations and fill gaps in the KMTX radar's coverage. Future work should include further investigation of winter storms precipitation gradients over small spatial and temporal scales in complex terrain using high-resolution numerical weather prediction models and dense surface observations, the continued development of an X-Band hydrometeor type algorithm for use with orographic precipitation and winter storms, and the implementation of gap-filling radar in an operational context.

REFERENCES

Allegretti, M., S. Bertoldo, and A. Prato, 2012: X-Band mini radar for observing and monitoring rainfall events. *Atmos. Climate Sci.*, **2**, 290–297.

Anders, A. M., G. H. Roe, D. R. Durran, and J. R. Minder, 2007: Small-scale spatial gradients in climatological precipitation on the Olympic Peninsula. *J. Hydrometeor.*, **8**, 1068–1081.

Benjamin, S. G., J. M. Brown, K. J. Brundage, B. E. Schwartz, T. G. Smirnova, T. L. Smith, and L. L. Morone, 1998: RUC-2 - The Rapid Update Cycle version 2. *NWS Tech. Procedures Bull. 448*.

Bond, N., B. Smull, M. Stoelinga, C. Woods, and A. Haase, 2005: Evolution of a cold front encountering steep quasi-2D terrain: Coordinated aircraft observations on 8-9 December 2001 during IMPROVE-2. *J. Atmos. Sci.*, **62**, 3559–3579.

Bousquet, O., and B. Smull, 2003: Airflow and precipitation fields within deep alpine valleys observed by airborne Doppler radar. *J. Appl. Meteor.*, **42**, 1497–1513.

Bruintjes, R., T. L. Clark, and W. D. Hall, 1994: Interactions between topographic airflow and cloud/precipitation development during the passage of a winter storm in Arizona. *J. Atmos. Sci.*, **51**, 48–67.

Colle, B., 2004: Sensitivity of orographic precipitation to changing ambient conditions and terrain geometries: An idealized modeling perspective. *J. Atmos. Sci.*, **61**, 588–606.

Colle, B., 2008: Two-dimensional idealized simulations of the impact of multiple windward ridges on orographic precipitation. *J. Atmos. Sci.*, **65**, 509–523.

Colle, B., C. Mass, and B. Smull, 1999: An observational and numerical study of a cold front interacting with the Olympic Mountains during COAST IOP5. *Mon. Wea. Rev.*, **127**, 1310–1334.

Colle, B., B. Smull, and M. Yang, 2002: Numerical simulations of a landfalling cold front observed during COAST: Rapid evolution and responsible mechanisms*. *Mon. Wea. Rev.*, **130**, 1945–1966.

Colle, B., J. Wolfe, W. Steenburgh, D. Kingsmill, J. Cox, and J. C. Shafer, 2005: High-resolution simulations and microphysical validation of an orographic precipitation event over the Wasatch Mountains during IPEX IOP3. *Mon. Wea. Rev.*, **133**, 2947–2971.

Colle, B. A., R. B. Smith, and D. A. Wesley, 2013: Theory, observations, and predictions of orographic precipitation. *Mountain Weather Research and Forecasting*, F.K. Chow, S.F.J. De Wekker, and B.J. Snyder, Eds., Springer Netherlands, Dordrecht, 291–344.

Cooper, W., and C. Saunders, 1980: Winter storms over the San Juan Mountains. Part II: Microphysical processes. *J. Appl. Meteor.*, **19**, 927–941.

Cox, J., W. Steenburgh, D. Kingsmill, J. Shafer, B. Colle, O. Bousquet, B. Smull, and H. Cai, 2005: The kinematic structure of a Wasatch Mountain winter storm during IPEX IOP3. *Mon. Wea. Rev.*, **133**, 521–542.

Crum, T., and R. Alberty, 1993: The WSR-88D and the WSR-88D Operational Support Facility. *Bull. Amer. Meteor. Soc.*, **74**, 1669–1687.

Daly, C., R. Neilson, and D. Phillips, 1994: A statistical-topographic model for mapping climatological precipitation over mountainous terrain. *J. Appl. Meteor.*, **33**, 140–158.

Dolan, B., and S. a. Rutledge, 2009: A theory-based hydrometeor identification algorithm for X-band polarimetric radars. *J. Atmos. Oceanic Technol.*, **26**, 2071–2088.

Durran, D., and J. Klemp, 1982: On the effects of moisture on the Brunt-Vaisala frequency. *J. Atmos. Sci.*, **39**, 2152–2158.

Egger, J. I., and K. P. Hoinka, 1992: Fronts and orography. *Meteor. Atmos. Phys.*, **36**, 3–36.

Frei, C., and C. Schär, 1998: A precipitation climatology of the Alps from high-resolution rain-gauge observations. *Int. J. Climatol.*, **18**, 873–900.

Garvert, M., B. Colle, and C. Mass, 2005: The 13-14 December 2001 IMPROVE-2 event. Part I: Synoptic and mesoscale evolution and comparison with a mesoscale model simulation. *J. Atmos. Sci.*, **62**, 3474–3492.

Garvert, M. F., B. Smull, and C. Mass, 2007: Multiscale mountain waves influencing a major orographic precipitation event. *J. Atmos. Sci.*, **64**, 711–737.

Gourley, J. J., D. P. Jorgensen, S. Y. Matrosov, and Z. L. Flamig, 2009: Evaluation of incremental improvements to quantitative precipitation estimates in complex terrain. *J. Hydrometeor.*, **10**, 1507–1520.

Gross, B., 1994: Frontal Interaction with isolated orography. *J. Atmos. Sci.*, **51**, 1480–1496.

Heggli, M., and R. Rauber, 1988: The characteristics and evolution of supercooled water in wintertime storms over the Sierra Nevada: A summary of microwave radiometric measurements taken during the Sierra Cooperative Pilot Project. *J. Appl. Meteor.*, **27**, 989–1014.

Hill, G., 1978: Observations of precipitation-forced circulations in winter orographic storms. *J. Atmos. Sci.*, **35**, 1463–1472.

Hobbs, P., 1975: The nature of winter clouds and precipitation in the Cascade Mountains and their modification by artificial seeding. Part I: Natural conditions. *J. Appl. Meteor.*, **14**, 783–804.

Horel, J., M. Splitt, and L. Dunn, 2002: MesoWest: Cooperative mesonets in the western United States. *Bull. Amer. Meteor. Soc.*, **83**, 211–225.

Houze, R., 2012: Orographic effects on precipitating clouds. *Reviews of Geophysics*, **50**, 1–47.

Houze, R., and S. Medina, 2005: Turbulence as a mechanism for orographic precipitation enhancement. *J. Atmos. Sci.*, **62**, 3599–3623.

Houze, R., C. James, and S. Medina, 2001: Radar observations of precipitation and airflow on the Mediterranean side of the Alps: Autumn 1998 and 1999. *Q. J. Roy. Meteor. Soc.*, **127**, 2537–2558.

James, C., S. Brodzik, H. Edmon, R. Houze, and S. Yuter, 2000: Radar data processing and visualization over complex terrain. *Wea. Forecasting*, **15**, 327–338.

Klimowski, B. A. and Coauthors, 1998: The 1995 Arizona Program: Toward a better understanding of winter storm precipitation development in mountainous terrain. *Bull. Amer. Meteor. Soc.*, **79**, 799–813.

Long, A., B. Campistron, and A. Huggins, 1990: Investigations of a winter mountain storm in Utah. Part I: Synoptic analyses, mesoscale kinematics, and water release rates. *J. Atmos. Sci.*, **47**, 1302–1322.

Marwitz, J., 1980: Winter storms over the San Juan Mountains. Part I: Dynamical processes. *J. Appl. Meteor.*, **19**, 913–926.

Medina, S., B. F. Smull, R. A. Houze, and M. Steiner, 2005: Cross-barrier flow during orographic precipitation events: Results from MAP and IMPROVE. *J. Atmos. Sci.*, **62**, 3580–3598.

Medina, S., E. Sukovich, and R. a. Houze, 2007: Vertical structures of precipitation in cyclones crossing the Oregon Cascades. *Mon. Wea. Rev.*, **135**, 3565–3586.

Minder, J. R., D. R. Durran, H. Roe, and A. M. Anders, 2008: The climatology of small-scale orographic precipitation over the Olympic Mountains: Patterns and processes. *Q. J. Roy. Meteor. Soc.*, **839**, 817–839.

Molinié, G., D. Ceresetti, S. Anquetin, J. D. Creutin, and B. Boudevillain, 2012: Rainfall regime of a mountainous Mediterranean region: Statistical analysis at short time steps. *J. Appl. Meteor. and Climatol.*, **51**, 429–448.

Murakami, M., and T. Matsuo, 1990: Development of the Hydrometeor Videosonde. *J. Atmos. Oceanic Technol.*, **7**, 613–620.

Neiman, P., and F. M. Ralph, 2004: Modification of fronts and precipitation by coastal blocking during an intense landfalling winter storm in southern California: Observations during CALJET. *Mon. Wea. Rev.*, **132**, 242–273.

Oye, R., C. Mueller, and S. Smith, 1995: Software for radar translation, visualization, editing, and interpolation. *27th AMS Conf. on Radar Meteorology*, Vail, CO, Amer. Meteor. Soc.

Peterson, T., L. Grant, W. R. Cotton, and D. Rogers, 1991: The effect of decoupled low-level flow on winter orographic clouds and precipitation in the Yampa River valley. *J. Appl. Meteor.*, **30**, 368–386.

Reinking, R., J. B. Snider, and J. L. Coen, 2000: Influences of storm-embedded orographic gravity waves on cloud liquid water and precipitation. *J. Appl. Meteor.*, **39**, 733–759.

Reynolds, D., and A. Kuciauskas, 1988: Remote and in situ observations of Sierra Nevada winter mountain clouds: Relationships between mesoscale structure, precipitation and liquid water. *J. Appl. Meteor.*, **27**, 140–156.

Rinehart, R., 1997: *Radar for Meteorologists*. 3rd Ed. Rinehart Publications, 428.

Roe, G. H., 2005: Orographic precipitation. *Annu. Rev. Earth Planet. Sci.*, **33**, 645–671.

Rotunno, R., and R. Houze, 2007: Lessons on orographic precipitation from the Mesoscale Alpine Programme. *Q. J. Roy. Meteor. Soc.*, **133**, 811–830.

Sassen, K., A. Huggins, A. B. Long, J. B. Snider, and R. J. Meitin, 1990: Investigations of a winter mountain storm in Utah. Part II: Mesoscale structure, supercooled liquid water development, and precipitation processes. *J. Atmos. Sci.*, **47**, 1323–1350.

Schneebeli, M., N. Dawes, M. Lehning, and A. Berne, 2013: High-resolution vertical profiles of X-band polarimetric radar observables during snowfall in the Swiss Alps. *J. Appl. Meteor. and Climatology*, **52**, 378–394, doi:10.1175/JAMC-D-12-015.1.

Schultz, D., and R. Trapp, 2003: Nonclassical cold-frontal structure caused by dry subcloud air in northern Utah during the Intermountain Precipitation Experiment (IPEX). *Mon. Wea. Rev.*, **131**, 2222–2246.

Schumacher, P., D. Knight, and L. Bosart, 1996: Frontal interaction with the Appalachian Mountains. Part I: A climatology. *Mon. Wea. Rev.*, **124**, 2453–2468.

Sinclair, M., D. Wratt, R. Henderson, and W. Gray, 1997: Factors affecting the distribution and spillover of precipitation in the Southern Alps of New Zealand-A case study. *J. Appl. Meteor.*, **36**, 428–442.

Smith, R., 2006: Progress on the theory of orographic precipitation. *Special Paper 398: Tectonics, Climate, and Landscape Evolution*, Geological Society of America, Boulder, CO, 1–16.

Smith, R. B., Q. Jiang, M. G. Fearon, P. Tabary, M. Dorninger, J. D. Doyle, and R. Benoit, 2003: Orographic precipitation and air mass transformation: An Alpine example. *Q. J. Roy. Meteor. Soc.*, **129**, 433–454.

Steenburgh, W., 2003: One hundred inches in one hundred hours: Evolution of a Wasatch Mountain winter storm cycle. *Wea. Forecasting*, **83**, 1018–1036.

Steiner, M., O. Bousquet, R. a. Houze Jr, B. F. Smull, and M. Mancini, 2003: Airflow within major Alpine river valleys under heavy rainfall. *Q. J. Roy. Meteor. Soc.*, **129**, 411–431.

Stoelinga, M. T., R. E. Stewart, G. Thompson, and J. Theriault, 2013: Microphysical processes within winter orographic cloud and precipitation systems. *Mountain Weather Research and Forecasting*, F.K. Chow, S.F.J. De Wekker, and B.J. Snyder, Eds., Springer Netherlands, Dordrecht, 345–408.

Vivekanandan, J., S. M. Ellis, R. Oye, D. S. Zrnic, a. V. Ryzhkov, and J. Straka, 1999: Cloud microphysics retrieval Using S-band dual-polarization radar measurements. *Bull. Amer. Meteor. Soc.*, **80**, 381–388.

Woods, C. P., M. T. Stoelinga, J. D. Locatelli, and P. V. Hobbs, 2005: Microphysical processes and synergistic interaction between frontal and orographic forcing of precipitation during the 13 December 2001 IMPROVE-2 event over the Oregon Cascades. *J. Atmos. Sci.*, **62**, 3493–3519.

Wurman, J., J. Straka, E. Rasmussen, M. Randall, and A. Zahrai, 1997: Design and deployment of a portable, pencil-beam, pulsed, 3-cm Doppler radar. *J. Atmos. Oceanic Technol.*, **14**, 1502–1512.

Yu, C., and B. Smull, 2000: Airborne Doppler observations of a landfalling cold front upstream of steep coastal orography. *Mon. Wea. Rev.*, 1577–1603.

2006: Little Cottonwood Canyon SR-210 Transportation Study. http://wfrc.org/Previous_Studies/ (Accessed July 16, 2013).

2013: Western Regional Climate Center (WRCC). *Cooperative Climatological Data Summaries*,. http://www.wrcc.dri.edu/climatedata/climsum/ (Accessed June 17, 2013).